The WISSH quasars project

II. Giant star nurseries in hyper-luminous quasars

F. Duras[1,2], A. Bongiorno[2], E. Piconcelli[2], S. Bianchi[3], C. Pappalardo[4,5], R. Valiante[2], M. Bischetti[2], C. Feruglio[6],
S. Martocchia[7], R. Schneider[8], G. Vietri[2], C. Vignali[9,10], L. Zappacosta[2], F. La Franca[1], and F. Fiore[2]

[1] Dipartimento di Matematica e Fisica, Università Roma Tre, via della Vasca Navale 84, 00146 Roma, Italy
   e-mail: federica.duras@oa-roma.inaf.it
[2] INAF–Osservatorio Astronomico di Roma, via Frascati 33, 00040 Monteporzio Catone, Italy
[3] INAF–Osservatorio Astrofisico di Arcetri, Largo E. Fermi, 5, 50125 Firenze, Italy
[4] Centro de Astronomia e Astrofísica da Universidade de Lisboa, Observatório Astronómico de Lisboa, 1349-017 Lisbona Tapada
   da Ajuda, Portugal
[5] Instituto de Astrofísica e Ciencias do Espaço, Universidade de Lisboa, OAL, Tapada da Ajuda, 1349-018 Lisboa, Portugal
[6] INAF–Osservatorio Astronomico di Trieste, via G. Tiepolo 11, 34124 Trieste, Italy
[7] Astrophysics Research Institute, Liverpool John Moores University, 146 Brownlow Hill, Liverpool L3 5RF, UK
[8] Dipartimento di Fisica Università di Roma La Sapienza, 00185 Roma, Italy
[9] Dipartimento di Fisica e Astronomia, Università di Bologna, viale Berti Pichat 6/2, 40127 Bologna, Italy
[10] INAF–Osservatorio Astronomico di Bologna, via Ranzani 1, 40127 Bologna, Italy

ABSTRACT

Context. Studying the coupling between the energy output produced by the central quasar and the host galaxy is fundamental to fully understand galaxy evolution. Quasar feedback is indeed supposed to dramatically affect the galaxy properties by depositing large amounts of energy and momentum into the interstellar medium (ISM).

Aims. In order to gain further insights on this process, we study the spectral energy distributions (SEDs) of sources at the brightest end of the quasar luminosity function, for which the feedback mechanism is assumed to be at its maximum, given their high efficiency in driving powerful outflows.

Methods. We modelled the rest-frame UV-to-far-IR SEDs of 16 WISE-SDSS Selected Hyper-luminous (WISSH) quasars at $1.8 < z < 4.6$ based on SDSS, 2MASS, WISE and *Herschel*/SPIRE data. Through an accurate SED-fitting procedure, we separate the different emission components by deriving physical parameters of both the nuclear component (i.e. bolometric and monochromatic luminosities) and the host galaxy (i.e. star formation rate, mass, and temperature of the cold dust). We also use a radiative transfer code to account for the contribution of the quasar-related emission to the far-IR fluxes.

Results. Most SEDs are well described by a standard combination of accretion disc plus torus and cold dust emission. However, about 30% of SEDs require an additional emission component in the near-IR, with temperatures peaking at $\sim$750 K, which indicates that a hotter dust component is present in these powerful quasars. We measure extreme values of both AGN bolometric luminosity ($L_{\rm BOL} > 10^{47}$ erg/s) and star formation rate (up to $\sim$2000 $M_\odot$/yr) based on the quasar-corrected, IR luminosity of the host galaxy. A new relation between quasar and star formation luminosity is derived ($L_{\rm SF} \propto L_{\rm QSO}^{0.73}$) by combining several *Herschel*-detected quasar samples from $z \sim 0$ to $\sim$4. WISSH quasars have masses ($\sim$10^8 $M_\odot$) and temperatures ($\sim$50 K) of cold dust in agreement with those found for other high-z IR luminous quasars.

Conclusions. Thanks to their extreme nuclear and star formation luminosities, the WISSH quasars are ideal targets to shed light on the feedback mechanism and its effect on the evolution of their host galaxies, as well as on the merger-induced scenario that is commonly assumed to explain these exceptional luminosities. Future observations will be crucial to measure the molecular gas content in these systems, probe the effect between quasar-driven outflows and on-going star formation, and reveal merger signatures in their host galaxies.

Key words. galaxies: active – galaxies: fundamental parameters – galaxies: star formation – quasars: general

1. Introduction

It has been a matter of hot debate in the past decades whether galaxy formation and the growth of supermassive black holes (SMBHs) are somehow connected to each other; if this connection is real, quasars play a crucial role in the evolutionary scenario. According to the latest models of galaxy-quasar co-evolution, the latter are capable to drive energetic outflows from the inner to the outer regions, during their active phase, which removes and/or heats up the molecular gas of the host galaxy out of which stars form. In this way, they stop both star formation (SF) and black hole (BH) accretion (see e.g. Silk & Rees 1998; Hopkins & Elvis 2010; Zubovas & King 2012; Costa et al. 2014). If this were true, quasars would act as a powerful quenching mechanism, that prevents massive galaxies from overgrowing and is responsible for the transition of their hosts from the blue cloud to the red sequence.

On the one hand, outflows have been largely observed and studied in the ionised gas component (Holt et al. 2008; Nesvadba et al. 2008; Rupke & Veilleux 2011; Carniani et al. 2015; Bischetti et al. 2017), while only a few cases are known of powerful outflows that involve the molecular gas

(Feruglio et al. 2010, 2013, 2015; Sturm et al. 2011; Cicone et al. 2012, 2014; Aalto 2015; González-Alfonso et al. 2017). It is in fact not yet clear how they are linked.

On the other hand, some models also require positive quasar feedback driven by the outflow, in the form of induced SF in the host galaxy, through gas compression of the interstellar medium (ISM, King 2005; Ishibashi & Fabian 2012; Silk 2013). However, very little observational evidence is available (Cano-Díaz et al. 2012; Cresci et al. 2015a,b; Maiolino et al. 2017), that would support this fascinating scenario.

Since the co-evolution of BHs and galaxies is directly linked to the SF rate (SFR) and consumption of gas, one of the key parameters to study is the SF activity of the quasar host galaxies. This has benefitted from progressively larger numbers of quasars being identified in wide, systematic infrared galaxy surveys. The problem in this type of analysis is that the quasar may bias the SF estimate in the host by contaminating the UV and optical range of the spectrum. A possible solution might be to use the far-infrared (FIR) emission, through UV light that is reprocessed by the dust grains. The quasar contamination drops towards the FIR band (see, however Schneider et al. 2015), and the effect of dust extinction is almost negligible.

The first investigations of the FIR emission in quasars was carried out with the Infrared Astronomical Satellite (IRAS) and the Infrared Space Observatory (ISO) combined with data from SCUBA and IRAM which extended the observational range at longer wavelengths. The launch of the *Herschel* Space Observatory in 2009 (Pilbratt et al. 2010) allowed us to observe the galaxy rest-frame emission as never before. Thanks to *Herschel* observations, several studies have been made in the past years to understand whether the presence of a quasar in the centre of the galaxy has any influence on the host SFR. The results have been contradictory, however. Most of these studies have found evidence for enhanced SFR in quasars hosts, compared to non-active galaxies of the same stellar mass, and argued that the bulk of moderate-luminosity X-ray selected quasars are hosted in galaxies that trace the normal star-forming main-sequence (MS) galaxies (e.g. Harrison et al. 2012; Mullaney et al. 2012b; Rosario et al. 2013; Santini et al. 2012; Stanley et al. 2015). Conversely, Bongiorno et al. (2012), Azadi et al. (2015), Mullaney et al. (2015) reported a broad specific SFR (sSFR) distribution for X-ray selected quasars that peak below the MS.

In addition, a further analysis is required to understand whether quasars are more likely to reside in quiescent or in star-forming host galaxies, that is, to search for an overall correlation between the SF and the nuclear activity in individual galaxies. Hatziminaoglou et al. (2010), studying a sample of *Herschel* Multi-tiered Extragalactic Survey (HerMES) high-redshift quasars, found a correlation between the quasar and the SF luminosities for both high- and low-luminosity sources. Shao et al. (2010), alternatively, showed a slight dependence on quasar luminosity for the SF in the latter class, in accordance with the results of Mullaney et al. (2012b) for moderate- luminous quasars and results of Rosario et al. (2012) who used a larger sample, including the COSMOS sample. Conversely, Mullaney et al. (2012a) did find hints of coeval growth of the super-massive BH and host galaxy, suggesting a causal connection, which was also found by Delvecchio et al. (2015) in their analysis of about 8500 sources with *Herschel* observations up to $z = 2.5$. A possible reason for such discrepant results resides in the fact that an additional question needs to be kept in mind, which is the strength of the quasar contamination in the FIR. Symeonidis (2017) argued that in their sample of

the most powerful quasars collected from Tsai et al. (2015) and Netzer et al. (2016), the total infrared luminosity was dominated by the quasar emission and there was no need for a star-forming component. On the contrary, Hatziminaoglou et al. (2010) showed that a starburst was always needed to reproduce the FIR emission of their sample. The truth is probably in between these two scenarios: Haas et al. (2003) proposed that objects hosting the highest FIR luminosities ($L_{FIR} > 10^{13}-10^{14} L_{\odot}$) have a strong star-forming component but the quasar contribution in the FIR is not negligible. Similarly, Dai et al. (2012) and Schneider et al. (2015) concluded that the radiation emitted by the central nucleus can provide an important source of heating for the dust in the galaxy.

In order to understand the discrepant results of the aforementioned works, it is important to constrain any correlation between the quasars and their host galaxy parameters. Models and observations have both confirmed that the efficiency in driving energetic winds and the momentum fluxes of galaxy-scale outflows increases with the quasar bolometric luminosity (see e.g. Menci et al. 2008; Hopkins et al. 2016; Fiore et al. 2017). Hence, we would expect that feedback could reach its maximum efficiency at the brightest end of the quasar luminosity function. For this reason, understanding the coupling between the nuclear energy output and the host galaxy is an open issue that is particularly relevant for the most luminous quasars, especially at $1 < z < 3$, the golden epoch for galaxy-quasar co-evolution.

For these reasons, we here present a multi-wavelength analysis of 16 quasars belonging to the wider WISSH (WISE-SDSS Selected Hyper-luminous) sample, which collects about 90 of the most luminous quasars known, with the highest bolometric luminosities, that is, $L_{BOL} \geq 10^{47}$ erg/s.

A detailed spectral energy distibution (SED) analysis was performed, from the UV to the FIR, in order to accurately separate the different emission components. The strength of the SED fitting method is that, given sufficiently wide photometric coverage, it is applicable to all quasars, obscured and unobscured, independently of their luminosity. Moreover, a detailed radiative transfer model was used in order to statistically assess the relative contribution to dust heating by the central quasar and the hot stars.

The paper is organised as follows: in Sect. 2 we describe the sample and the data, with the focus on the *Herschel* data extraction procedure. Section 3 provides a detailed explanation of the method we used to separate the different emission components, and we describe the templates we adopted to model the whole spectral energy distribution. The result of the fitting procedure is shown in Sect. 4, where we report bolometric and monochromatic luminosities and a study of the infrared properties (host infrared luminosity and SFR, cold and hot dust masses) of the sources. In the same section we also thoroughly study the possible contribution of the quasar to the FIR fluxes, from which we gain a statistical result that can be be applied to the entire sample. Finally, Sect. 5 presents the conclusions of our work.

In what follows, we adopt a ΛCDM cosmology with $H_0 = 67.90$ km s^{-1}/Mpc, $\Omega_m = 0.3065$, $\Omega_\Lambda = 0.6935$ (Planck Collaboration XIII 2016).

2. Sample and data

In this paper, we focus on a sub-sample of 16 quasars at $1.9 < z < 4.6$ extracted from the WISSH quasar sample. The total WISSH sample (see Bischetti et al. 2017, hereafter Paper I, for more details) includes 86 quasars that were obtained by cross-correlating the sources detected at 22 μm with a flux

Table 1. Sample of WISSH quasars.

N	SDSS name	z	Prop *Herschel* ID	Reference
1	SDSSJ012403.77+004432.6	3.840	OT2_mviero_2	Viero et al. (2014)
2	SDSSJ020950.71–000506.4	2.856	OT2_mviero_2	Viero et al. (2014)
3	SDSSJ073502.30+265911.5	1.982	OT2_dweedman_2	Weedman & Sargsyan (2016)
4	SDSSJ074521.78+473436.1	3.225 *	OT2_dweedman_2	Weedman & Sargsyan (2016)
5	SDSSJ080117.79+521034.5	3.263 *	OT2_dweedman_2	Weedman & Sargsyan (2016)
6	SDSSJ081855.77+095848.0	3.694	OT2_dweedman_2	Weedman & Sargsyan (2016)
7	SDSSJ090033.50+421547.0	3.294 *	OT2_dweedman_2	Weedman & Sargsyan (2016)
8	SDSSJ092819.29+534024.1	4.390	OT2_dweedman_2	Weedman & Sargsyan (2016)
9	SDSSJ101549.00+002020.0	4.400	OT1_vkulkarn_1	Not published
10	SDSSJ121549.81–003432.1	2.707	KPOT_seales01_2	Eales et al. (2010)
11	SDSSJ123714.60+064759.5	2.781	KPOT_jdavie01_1	Davies et al. (2012)
12	SDSSJ125005.72+263107.5	2.044	KPOT_seales01_2	Eales et al. (2010)
13	SDSSJ143352.20+022713.9	4.620	OT1_hnetzer_2	Netzer et al. (2014)
14	SDSSJ170100.60+641209.3	2.737	OT2_ymatsuda_1	Kato et al. (2016)
15	SDSSJ212329.46–005052.9	2.283 *	OT2_hnetzer_4	Netzer et al. (2014)
16	SDSSJ234625.66–001600.4	3.512 *	GT2_mviero_1	Viero et al. (2014)

Notes. The table includes: source number, SDSS ID, SDSS redshift (the z of sources with an asterisk was obtained by Vietri et al. (in prep.), from LBT NIR spectroscopy or SINFONI spectroscopy) and *Herschel* Proposal IDs (with relative publication where present).

density $S_{22\,\mu m} > 3$ mJy from the Wide-field Infrared Explorer (WISE Wright et al. 2010) with the Sloan Digital Sky Survey (SDSS) DR7 optically discovered type I sources at $z > 1.5$. The mid-IR $22 - \mu$m selection of the WISSH sample offers several benefits. In particular, (1) IR-loud sources that could be lost in UV-selected samples are favoured and we tend to select quasars that represent, as some prominent models predict (see e.g. Sanders et al. 1988; Hopkins et al. 2006, 2008), an intermediate population emerging from the merger-driven, heavily obscured phase that precedes the blue quasar phase in which the gas and dust content in the host galaxy may be already swept away; (2) all quasars can be compared in IR luminosity without the typical uncertainties due to extinction correction that affects the luminosity measurements at shorter wavelengths.

WISSH quasars populate the brightest end of the luminosity function, as visibile in Fig. 1, where we show the $L_{\rm bol}$ vs. z distribution of the total WISSH sample (in blue), compared to the COSMOS survey by Bongiorno et al. (2012) in grey and the PG quasars by Veilleux et al. (2009) and Petric et al. (2015) in green.

This work focusses on the 16 quasars of the WISSH sources for which *Herschel* observations are available on the archive. The lack of a unique preselection in the observational campaigns from which the data have been extracted reduces possible selectiones bias. Moreover, as shown in Fig. 1, the large stars appear to be randomly distributed in both redshift and luminosity. They could therefore be considered representative of the total WISSH sample. For these 16 quasars the bolometric luminosity was computed as explained in Sect. 4.1 while for the remaining 70 sources we used the SED-fitting analysis by Duras et al. (in prep.).

For all the analysed sources we have data in the three *Herschel* SPIRE bands (at $250\,\mu$m, $350\,\mu$m and $500\,\mu$m). They are ideal targets to study host properties such as the SFR, IR luminosities and dust masses, and we relate them to the nuclear properties, such as BH accretion and quasar bolometric luminosities.

In Table 1 we list the 16 sources studied here, reporting the numeric ID associated with each source, their SDSS ID, and their redshift. The redshift of most objects is taken from
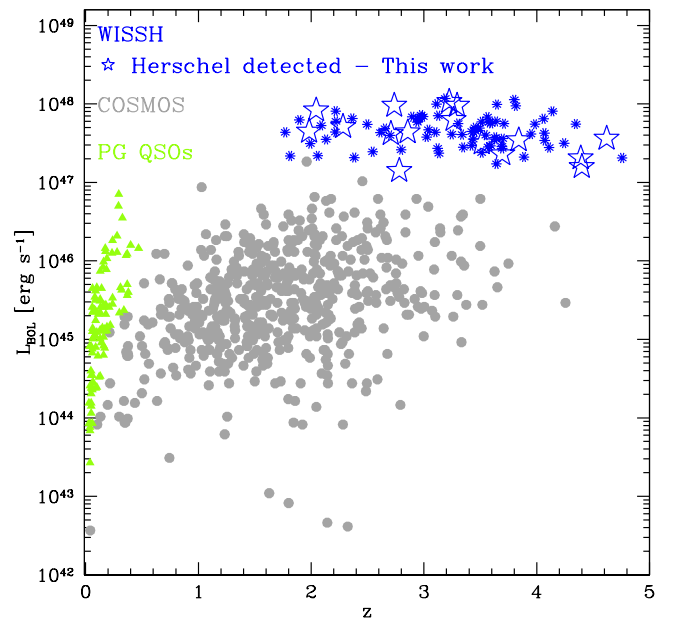
Fig. 1. Bolometric luminosity versus redshift of the total WISSH sample (in blue). The large stars are the 16 sources with *Herschel* data. For comparison, the COSMOS survey by Bongiorno et al. (2012) and the PG QSOs by Veilleux et al. (2009) and Petric et al. (2015) are shown in grey and green, respectively.

the seventh or the tenth release of the SDSS, but for 5 of the 16 sources, we can rely on the more accurate z estimates performed by Vietri et al. (in prep.) on LBT/LUCI spectra using the Hβ line.

2.1. Multi-wavelength data

For the 16 sources analysed here, we collected data from four different surveys for a total of 15 bands: SDSS covering the optical bands u, g, r, i and z[1]; 2MASS in the NIR J, H, and K bands[2], WISE at $3\,\mu$m, $4.5\,\mu$m, $12\,\mu$m, and $22\,\mu$m and

---

[1] http://skyserver.sdss.org/dr10/en/home.aspx
[2] http://irsa.ipac.caltech.edu/frontpage/

Table 2. Summary of the photometric survey properties.

Survey/instrument	Filter	λ_{eff}
SDSS	u	3543 Å
	g	4770 Å
	r	6231 Å
	i	7625 Å
	z	9134 Å
2MASS	J	12 350 Å
	H	16 620 Å
	K	21 590 Å
WISE	W1	3.35 μm
	W2	4.60 μm
	W3	11.56 μm
	W4	22.08 μm
Herschel	SPIRE1	243 μm
	SPIRE2	340 μm
	SPIRE3	482 μm

finally SPIRE in the FIR, at 250 μm, 350 μm, and 500 μm. All the photometric data were corrected for Galactic extinction (Schlegel et al. 1998).

In Table 2, we report the effective wavelengths of the filters, while the magnitudes from the UV to the MIR of the sample are shown in Table 3.

While for the UV-to-NIR data we collected the data from published catalogues, the photometry in the FIR bands was extracted from archival data.

2.1.1. *Herschel* SPIRE data: source extraction

For the FIR photometry we used *Herschel* archival data as specified in Table 1. For each source we estimated the *Herschel* flux densities at SPIRE wavelengths using the `sourceExtractorTimeline` (Bendo et al. 2013), a fitting method implemented in HIPE (Ott 2010), which is widely used for point-like sources (see for example Pappalardo et al. 2016; Ciesla et al. 2012). *Herschel* observations are performed by orthogonally scanning each target with the SPIRE bolometers, measuring the fluxes at regular time intervals. The measurement set of the bolometers for each cross-scan is called "timeline" data. The `sourceExtractorTimeline` fits these timeline data from all bolometers within an individual array with a two-dimensional Gaussian function. The input is the source position, a radius containing the source, and an aperture identifying the background annulus. Following the prescriptions of Pappalardo et al. (2015), we set a search radius for the target of 22″, 30″, and 42″, at 250 μm, 350 μm, and 500 μm, respectively. For the background annulus we define a set of different apertures between 140″ and 220″, and we estimate the background from the median of all the values recovered.

Following Pappalardo et al. (2015), two fits were performed to the timeline data. The first fit was performed using a circular Gaussian function in which the FWHM was allowed to vary. Then the FWHM was used to determine whether the source is resolved or unresolved and to reject sources that are either too narrow (which may be unremoved glitches) or too broad (which are probably extended sources). To test at which distance two

sources are distinguishable, point-like objects with the same flux density and an increasing distance from each other were injected in the timeline data. We found that two sources are resolved only if they are at a distance above ~22″, 30″, and 46″ at 250, 350, and 500 μm, respectively. Fixing the distance between the sources to these values, as a second step, we injected point-like objects at different flux densities in the timeline data to investigate the FWHM recovered by sourceExtractorTimeline. These tests demonstrate that artificial sources with FWHM corresponding to the telescope beam (17.5″, 23.9″, and 35.1″ at 250, 350, and 500 μm, respectively) added to timeline data may have an FWHM between 10″ and 30″ at 250 μm, 13.3″ and 40″ at 350 μm, and 20″ and 60″ at 500 μm. Therefore, sources, whose FWHM was determined via sourceExtractorTimeline and were outside these values were excluded from the analysis.

Although other software packages have been developed for source extraction within complex extragalactic fields (including software developed specifically for *Herschel*), we prefer to use the timeline fitter because the SPIRE data are flux calibrated at the timeline level using timeline-based point-spread function-fitting techniques, so that the method that we used is consistent with the flux calibration measurements themselves and is therefore expected to be more accurate.

In Table 4 we report the photometric flux densities obtained from the images.

3. UV-to-FIR spectral energy distribution

In this section, we describe the tool we developed to study the SED of our sources. The approach is based on the idea that the overall observed SED of each quasar is the result of the combination of different components that can be separated, that is, the nuclear emission and the galactic stellar light. The nuclear emission is characterised by two bumps in the UV and NIR regimes (Sanders et al. 1989; Elvis et al. 1994; Richards et al. 2006), which create a dip at around 1 μm. The UV bump is due to thermal emission from the accretion disc (Czerny & Elvis 1987), while the NIR bump is due to the intrinsic primary radiation absorbed by hot dusty clouds in the torus that is subsequently re-emitted at longer wavelength. In the same way, the galactic stellar light is made of a combination of direct UV emission by hot stars and its re-emission in the FIR through the reprocessed light by the cold dust component that is present at galactic scales. These components are described in more detail in Sect. 3.2.

3.1. Modelling the whole SED using a multi-component fitting procedure

The approach we followed is based on a three-component fitting procedure that in turn is based on the weighted least-square method, better known as the standard reduced χ^2 minimization, where the reduced χ^2 is in the form

$$\chi_\nu^2 = \frac{1}{n-p} \sum_{i=1}^{n} \left(\frac{f_i^{\text{obs}} - f_i^{\text{model}}}{\sigma_i} \right)^2 \tag{1}$$

with n the observed data points, f_i^{obs} and σ_i the observed fluxes and associated errors of the photometric bands, f_i^{model} the total flux of the chosen model with p free parameters, and $\nu = n - p$ the degrees of freedom.

Our model (f_{model}) includes three emission components:

$$f_{\text{model}} = A\, f_{\text{AD}+T} + B\, f_{\text{CD}} + C\, f_{\text{NE}} \tag{2}$$

Table 3. UV to MIR photometry for the sample.

N	u	g	r	i	z	J	H	K	W1	W2	W3	W4
1	23.23	19.18	17.86	17.92	17.82	17.68	17.28	17.55	17.13	17.35	15.80	14.35
	±0.51	±0.01	±0.01	±0.01	±0.02	±0.15	±0.16	±0.22	±0.03	±0.04	±0.09	±0.17
2	18.35	17.14	17.05	16.93	16.81	16.64	16.68	16.77	16.50	16.12	14.45	13.45
	±0.02	±0.01	±0.01	±0.01	±0.01	±0.06	±0.12	±0.13	±0.02	±0.03	±0.09	±0.07
3	16.62	16.44	16.22	16.03	15.89	15.90	15.89	15.69	15.59	14.99	13.51	12.78
	±0.01	±0.01	±0.01	±0.01	±0.01	±0.03	±0.04	±0.04	±0.02	±0.02	±0.02	±0.06
4	19.22	16.38	16.17	16.15	16.09	15.91	15.94	15.95	15.80	15.81	14.57	13.79
	±0.03	±0.01	±0.01	±0.01	±0.01	±0.04	±0.05	±0.05	±0.02	±0.02	±0.04	±0.10
5	19.49	17.08	16.77	16.66	16.62	16.58	16.70	16.44	16.52	16.34	14.45	13.69
	±0.03	±0.01	±0.01	±0.01	±0.01	±0.07	±0.13	±0.10	±0.03	±0.03	±0.03	±0.09
6	24.98	19.01	17.84	17.79	17.70	17.59	<17.30	17.63	17.53	17.64	15.49	14.40
	±0.71	±0.01	±0.01	±0.01	±0.02	±0.15	–	±0.22	±0.03	±0.05	±0.07	±0.20
7	22.84	17.01	16.68	16.63	16.54	16.24	16.04	15.89	15.87	15.60	14.74	13.89
	±0.38	±0.01	±0.01	±0.01	±0.01	±0.07	±0.07	±0.06	±0.02	±0.02	±0.04	±0.11
8	24.48	23.59	20.28	19.46	18.53	18.09	17.89	17.70	17.85	17.96	16.24	14.72
	±0.92	±0.32	±0.03	±0.02	±0.03	±0.21	±0.27	±0.24	±0.03	±0.05	±0.11	±0.20
9	24.12	21.68	19.62	19.20	18.93	–	–	–	18.20	18.29	16.55	15.17
	±0.68	±0.06	±0.02	±0.02	±0.04	–	–	–	±0.05	±0.11	±0.29	±0.52
10	18.96	17.43	17.28	17.09	16.87	16.69	16.64	16.65	16.49	16.13	14.19	13.34
	±0.02	±0.01	±0.01	±0.01	±0.01	±0.07	±0.07	±0.12	±0.03	±0.03	±0.04	±0.09
11	21.24	19.11	18.53	18.33	18.18	–	–	–	17.33	16.93	14.95	13.74
	±0.10	±0.01	±0.01	±0.01	±0.02	–	–	–	±0.03	±0.04	±0.05	±0.11
12	15.52	15.58	15.52	15.34	15.19	15.24	15.22	15.03	15.17	14.77	13.36	12.68
	±0.01	±0.01	±0.01	±0.01	±0.01	±0.04	±0.05	±0.04	±0.02	±0.02	±0.02	±0.05
13	22.64	21.61	19.42	18.25	18.18	17.43	17.56	17.43	17.78	17.61	15.89	14.58
	±0.43	±0.07	±0.02	±0.01	±0.03	±0.16	±0.01	±0.22	±0.03	±0.05	±0.08	±0.18
14	16.61	15.96	15.87	15.79	15.73	15.64	15.68	15.77	15.70	15.49	13.88	13.09
	±0.01	±0.01	±0.01	±0.01	±0.01	±0.05	±0.04	±0.05	±0.02	±0.02	±0.02	±0.04
15	16.94	16.47	16.30	16.25	16.04	16.05	15.98	15.74	16.01	15.51	13.95	13.11
	±0.01	±0.01	±0.01	±0.01	±0.01	±0.05	±0.07	±0.06	±0.02	±0.02	±0.01	±0.06
16	21.03	18.53	17.79	17.67	17.50	17.74	17.50	17.14	17.25	17.26	15.59	14.26
	±0.07	±0.01	±0.01	±0.01	±0.01	±0.16	±0.18	±0.16	±0.03	±0.05	±0.08	±0.17

Notes. Magnitudes are in the AB system.

where f_{AD+T} represents the emission coming from the accretion disc (both direct and reprocessed by the dusty torus), f_{CD} accounts for the FIR emission due to the reprocessed flux by cold dust and is modelled as a modified blackbody, f_{NE} is any possible NIR emission excess modelled with a simple blackbody. Finally, A, B, and C are the relative normalisations. For each component we have created a library of templates described below. The fitting procedure, through χ^2 minimisation, allows us to determine the combination of templates that best describes the observed SED and their relative contribution.

3.2. Library templates

The data were fitted with three main emission components (see previous section). For each component, a number of templates spanning a large grid of physical parameters were created. In the next sections we describe them in detail.

3.2.1. Quasar emission

The first component of the SED-fitting tool includes the direct emission from the central engine and the light absorbed and re-emitted by the dusty torus.

Nuclear emission

The shape of the SED of the primary source is commonly described by power laws of different spectral indices that vary considerably from one work to another, however. In order to evaluate the best shape to describe the observed emission of a generic quasar, we analysed different models of UV emission that are used in literature.

Fritz et al. (2006) modelled the primary source of emission, which was updated by Stalevski et al. (2012, 2016), as a composition of power laws with indices from Granato & Danese (1994)

Table 4. FIR flux densities in the three *Herschel*-SPIRE bands for the WISSH quasars.

N	$f_{250\,\mu m}$ [mJy]	$f_{350\,\mu m}$ [mJy]	$f_{500\,\mu m}$ [mJy]
1	<48	<44	<40
2	71 ± 18	61 ± 10	31 ± 10
3	91 ± 7.2	53 ± 7.3	33 ± 9.2
4	55 ± 7.4	58 ± 7.3	52 ± 9.5
5	93 ± 7.3	80 ± 8.1	57 ± 10
6	48 ± 7.2	49 ± 7.3	<56
7	29 ± 7.7	19 ± 7.4	<27
8	65 ± 7.7	75 ± 8.2	66 ± 9.8
9	20 ± 5.2	23 ± 5.1	19 ± 6.6
10	75 ± 12	58 ± 12	51 ± 8.3
11	93 ± 5.1	94 ± 5.1	62 ± 6.4
12	<45	<31	<65
13	28 ± 2.9	23 ± 2.9	16 ± 3.6
14	81 ± 3.0	56 ± 2.9	<40
15	36 ± 3.7	28 ± 3.6	18 ± 4.5
16	41 ± 14	38 ± 9.9	<35

and Nenkova et al. (2002),

$$\lambda L_\lambda = \begin{cases} \lambda^{1.2} & 0.001 \le \lambda \le 0.030 \ [\mu m] \\ \lambda^0 & 0.030 < \lambda \le 0.125 \ [\mu m] \\ \lambda^{-0.5} & 0.125 < \lambda \le 20.0 \ \ [\mu m]. \end{cases} \quad (3)$$

Feltre et al. (2012) proposed an updated version of this model, changing the spectral indices of the power laws according to Schartmann et al. (2005), making them steeper at short wavelengths:

$$\lambda L_\lambda = \begin{cases} \lambda^{2} & 0.001 \le \lambda \le 0.050 \ [\mu m] \\ \lambda^{1.8} & 0.050 < \lambda \le 0.125 \ [\mu m] \\ \lambda^{-0.5} & 0.125 < \lambda \le 10.0 \ \ [\mu m] \\ \lambda^{-3} & \lambda > 10.0 \qquad\quad [\mu m]. \end{cases} \quad (4)$$

Figure 2 shows the aforementioned models from Stalevski et al. (2012) and Feltre et al. (2012) compared to the models derived from the composite quasar spectra by Telfer et al. (2002) and Stevans et al. (2014) based on HST quasars spectra and compared to the empirical SDSS quasar mean spectra from Richards et al. (2006) and Krawczyk et al. (2013). As visible in Fig. 2, the slope of Stalevski's power law at short wavelengths ($\lambda < 0.125\,\mu m$) seems to be at odds with all the other emission models, both empirical and theoretical ones. In our library of templates, we therefore chose to model the accretion disc emission using the recipe by Feltre et al. (2012).

Torus emission

Several models for the radiation that is emitted by the dusty torus surrounding the accretion disc are available in the literature, and they often result in very different solutions when fitted to the data. Feltre et al. (2012) studied the differences between a smooth and clumpy dusty torus by comparing the works by Fritz et al. (2006) and Nenkova et al. (2008). They concluded that the models with only a smooth grain distribution are not a realistic description of the torus, since they imply a large number of collisions that would raise the temperature so high that it would destroy the dust grains (see also Krolik & Begelman 1988). However, as a result of the difficulties in handling clumpy media and the lack of computational power, smooth models
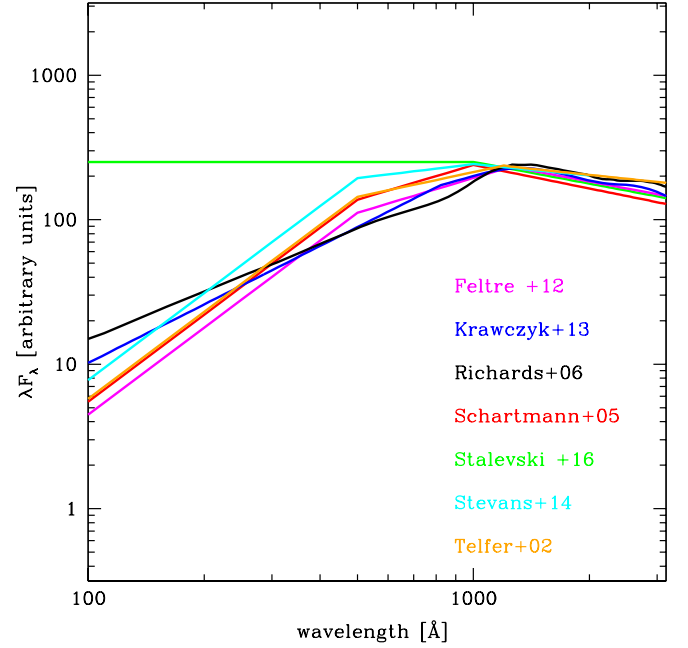
Fig. 2. Comparison of the SED for different emission models of the quasar primary source.

were used at first. Using a Monte Carlo radiative transfer code (SKIRT), Stalevski et al. (2012, 2016) simulated a dusty torus as a three-dimensional two-phase medium made of a combination of high-density clumps and low-density medium filling the space between the clumps. The models have been obtained starting from the smooth models by Fritz et al. (2006) and applying the algorithm described by Witt & Gordon (1996) to generate a two-phase clumpy medium, according to which each individual cell in the grid is assigned randomly, by a Monte Carlo process, to either a high- or a low-density state. In these models, the dust is a mixture of silicate and graphite grains (as in Mathis et al. 1977) with optical properties from Laor & Draine (1993) and Li & Draine (2001). Its distribution is described by a flared disc whose geometry is defined by the inner (R_{in}) and the outer (R_{out}) radii, and by the half-opening angle OA, which measures the dust-filled zone, from the equator to the edge of the torus, which is linked to the covering factor.

Of the other models of dusty tori, we considered the model by Hönig & Kishimoto (2010), which is similar to Stalevski's in that it uses a three-dimensional transfer code based on a Monte Carlo approach. However, the model proposed by Stalevski et al. (2012, 2016) provides the best description of the reprocessed emission by the torus, being both smooth and clumpy, and therefore it represents the best choice to constrain the IR part of the spectrum of our sources with high accuracy.

Of the available empirical infrared quasar SEDs, we compared our choice of the torus emission with the SEDs proposed by Netzer et al. (2007), Mor & Netzer (2012), Netzer et al. (2016) (an extended version of Mor & Netzer 2012, template at longer wavelenghts), and Symeonidis et al. (2016); these are shown in Fig. 3 in cyan, red, black and magenta respectively. Except for the SED proposed by Symeonidis et al. (2016), our torus model (in green) is in good agreement with all models. As described in more detail in Sect. 4.3, we found SFR values consistent with those published by Netzer et al. (2016) for three sources in common between the two samples, although different tori templates have been adopted. Focusing on the longest wavelengths, the empirical SED by Symeonidis et al. (2016) shows
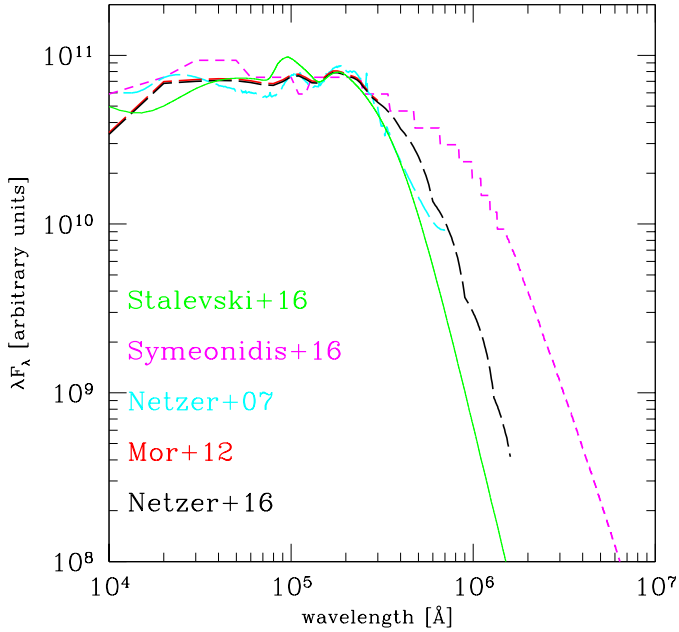
Fig. 3. Infrared torus model by Stalevski et al. (2016) compared with the empirical SEDs by Netzer et al. (2007), Mor & Netzer (2012), Netzer et al. (2016), and Symeonidis et al. (2016).

a much higher contribution (lower temperature) than the others. The reason probably is that in Symeonidis et al. (2016) the torus extent is larger than in the other cases. From a theoretical point of view, a huge radius of the torus (as the one described by Symeonidis et al. 2016) should predict a height of the torus itself that is difficult to support. Moreover, as recently pointed out by Lani et al. (2017), the discrepancy found between the mean SED by Symeonidis et al. (2016) and the other tori templates shown, might be due to the fact that the first has been obtained without normalising the individual SEDs at a given wavelength and, above all, that it does not represent the entire quasar population but rather the extremely IR-luminous ones.

In view of the above, for this work we created new templates accounting for the accretion disc plus torus emission, made by the combination of the quasar torus emission from Stalevski et al. (2016) and the nuclear emission from Feltre et al. (2012), appropriately normalised to preserve the energy balance between the UV and the IR bands.

This library is made of 1920 templates with different values of optical depth τ at 9.7 μm, half-opening angle OA, and dust distribution. In addition, each of them has ten different lines of sight θ, from face-on (0°, for typical unobscured type I AGN) to edge-on (90°, obscured type II AGN) view, for a total of 19 200 templates (in Fig. 4 torus templates for different varying parameters are shown). However, in order to reduce the computational time, we used only those with inclination angle 0°, which is a reasonable assumption considering that we study type I AGN and that the inclination angle i and the optical depth τ are strongly degenerate. In this way, we obtained a reduced library of 1920 templates of accretion disc plus torus.

3.2.2. Cold dust emission

The second component of the SED-fitting procedure is a modified blackbody accounting for the emission powered by SF, which is absorbed by dust grains and re-emitted in the MIR and FIR. We know that the stellar light is emitted in the UV-to-NIR

bands of the spectrum, with the NIR dominated by the older stars, while the UV is dominated by the massive short-lived stars. The same stars are responsible for polluting the ISM with metals and dust, producing grains that absorb the stellar light and re-radiate it in the IR and submillimiter domains.

In the far-infrared, this dust emits thermal emission that is characterised by a blackbody spectrum with an additional $\lambda^{-\beta}$ term that accounts for the emissivity of the dust (Hildebrand 1983). It must be stressed that since the FIR emission is produced by a mixture of grains of different shapes and sizes, this results in a distribution of temperatures. For simplicity, we can assume a single-temperature modified blackbody emission even if the SEDs of real galaxies are obviously more complex. Following Blain et al. (2002), the rest-frame emission of this cold dust is modeled as:

$$\mathrm{MBB}(T_{\mathrm{CD}}, \lambda) = \lambda^{-\beta}\,\mathrm{BB}(T_{\mathrm{CD}}, \lambda) \qquad (5)$$

where $\mathrm{BB}(T_{\mathrm{CD}}, \lambda)$ is the Planck function for a dust temperature T_{CD} and β is the emissivity index. The temperature of the modified blackbody and the normalisation are free parameters.

The emissivity of dust grains is generally taken to be a power law at these long wavelengths, with models and laboratory data suggesting indices ranging from $1 \leq \beta \leq 2$. One of the main sources of uncertainty lies in the exact determination of this value: different values of β produce a systematic change in the best-model value of T_{CD} since a smaller β implies a higher cold dust temperature. Following Beelen et al. (2006), we fixed β to 1.6, which seems to be the most appropriate value for high-z quasars. Recently, works based on Planck and *Herschel* data have shown that the value of $\beta = 1.6$ (instead of $\beta = 2.0$ used in the past) might be the most correct to also describe the dust in local galaxies; see for example the studies on the Milky Way by Bianchi et al. (2017) and Sect. 4.3 of Planck Collaboration XI (2014).

The cold dust library consists of about 50 BB templates, with temperatures in the range $20\,\mathrm{K} < T < 70\,\mathrm{K}$.

3.2.3. NIR emission excess

As outlined by several authors in the past, and shown in Fig. 7, an additional component in the near-infrared is often required to fit the NIR part of the SED of luminous quasars (see Barvainis 1987; Mor et al. 2009; Leipski et al. 2013).

In the works mentioned above, the authors speculated that the dust grains are probably made of pure graphite since they are able to survive to temperatures higher than the silicate temperatures present in the torus (Minezaki et al. 2004; Suganuma et al. 2006). The physical scale of this hot dust is delimited by the sublimation radius of "typical" dust composed of both silicate and graphite grains (torus inner radius) and the sublimation radius of pure graphite grains (which has a sublimation temperature of $\sim$1500 K).

To describe the NIR emission excess, we generated about 650 templates using blackbodies of different temperatures, from $T_{\mathrm{NE}} = 190\,\mathrm{K}$ to $T_{\mathrm{NE}} = 1800\,\mathrm{K}$.

4. Results of the SED fitting

Given the wide multi-wavelength coverage, the fitting technique described above allows us to decompose the entire spectral energy distribution into the different emission components and to derive robust measurements of both the quasar and the host galaxy properties. In Figs. 5 and 6 we show the best-fit SED
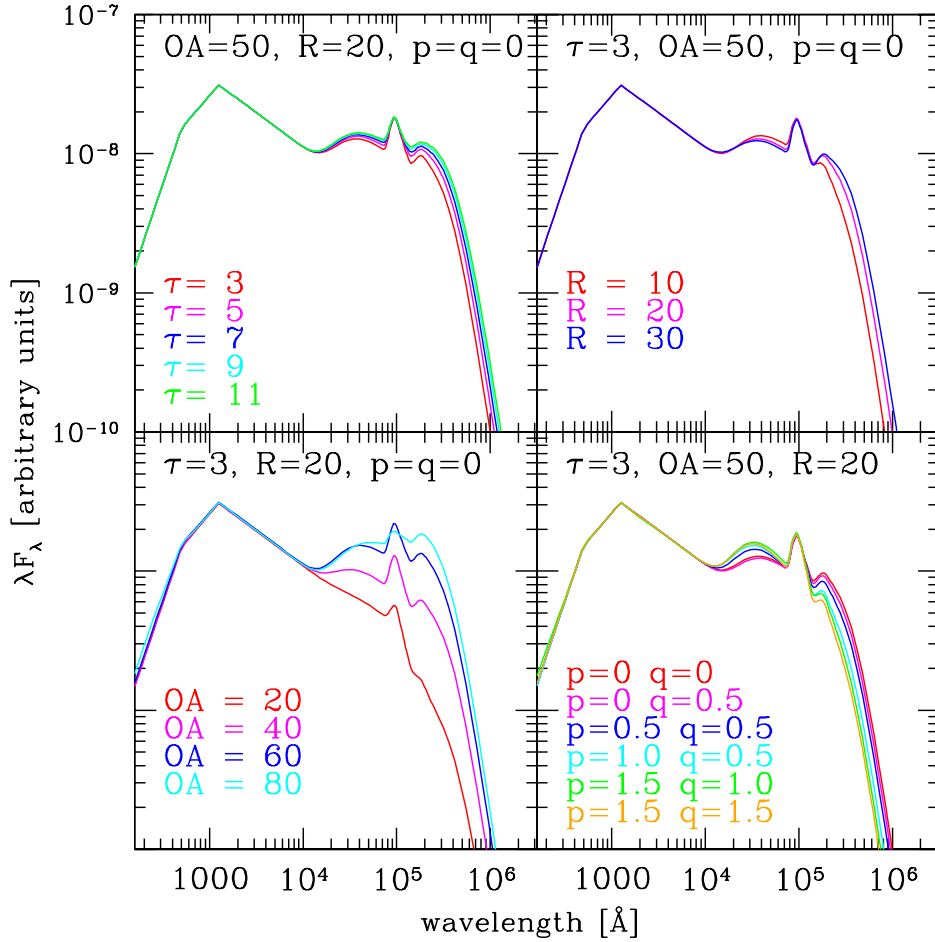
Fig. 4. Examples of templates at inclination angle $i = 0°$ used to describe the AD plus T emission. Different panels show how the torus emission changes when the physical parameters are varied, i.e. optical depth τ, ratio of outer to inner radius $R = R_{out}/R_{in}$, half-opening angle OA, and the p and q parameters related to the density gradient along the radial direction and with polar angle $\rho(r, \theta) \propto r^{-p}e^{-q|cos\theta|}$ (Granato & Danese 1994).

model for the 16 sources. Black circles are the rest-frame photometric points corresponding to the observed bands we used to constrain the SED. Data below 1216 Å corresponding to the Lyman-α emission line, are plotted as open circles and are not taken into account in the fit. At these wavelengths, the flux is expected to be weakened due to the Lyman α absorption forest, which is not included in our model. Data points above 1216 Å were fitted with a combination of the components described above. In detail: (i) accretion disc plus torus emission (AD + T, blue line with cyan shaded area); (ii) cold dust emission in the IR band (CD, red line with orange shaded area); and (iii) NIR excess when necessary (NE, green line with shaded area). The shaded areas describe the range of values corresponding to the solutions for which $\Delta\chi^2 = \chi^2(\text{sol}) - \chi^2(\text{best}) \leq 1.0$, 1σ in the case of one parameter of interest (see Avni 1976).

As a first step, we considered a standard combination of AD + T and CD components in the fit. However, in a few cases we found that these models are not enough to reproduce the whole SED, which shows an excess of emission in the NIR bands. For these cases, we therefore added as a third component, the additional NIR excess template, while fixing the AD + T and CD best-emission models found in the first run.

To quantify whether such a component really does improve the fit, we performed the F-test, which measures the goodness of two nested models through the comparison of the χ^2 and degrees of freedom obtained in the two cases.

Figure 7 shows as an example, one of the sources for which the additional component was added (SDSSJ123714.60+064759.5). As visible even by eye, the inclusion of the NIR excess component improves the fit: the WISE 3 photometric point shows that including the NIR excess component brings the fit a factor of ∼5 closer to the observed point. For SDSSJ123714.60+064759.5, the result of the F-test is $F = 16.67$, meaning that the addition of the third component produces an improvement in the resulting fit statistic that is significant at a confidence level ≥99%. In the whole sample, we found that the NIR excess blackbody component is required in 5 out of the 16 sources (∼31%).

### 4.1. Bolometric and monochromatic luminosities

From the final SED best-fit, we derived several physical quantities of both the host galaxy and the nuclear source. The intrinsic quasar bolometric luminosity was computed for each source by integrating the accretion disc emission in the range 60 Å−1 μm (although Figs. 5 and 6 only show wavelengths above ∼500 Å).

In particular,

$$L_{\text{bol}} = 4\pi d_L^2 \int_{60\,\text{Å}}^{1\,\mu\text{m}} A\,f_{\text{AD}}\ \ [\text{erg/s}] \quad (6)$$

where d_L is the luminosity distance and f_{AD} is the accretion disc emission component with A relative normalisation. In the
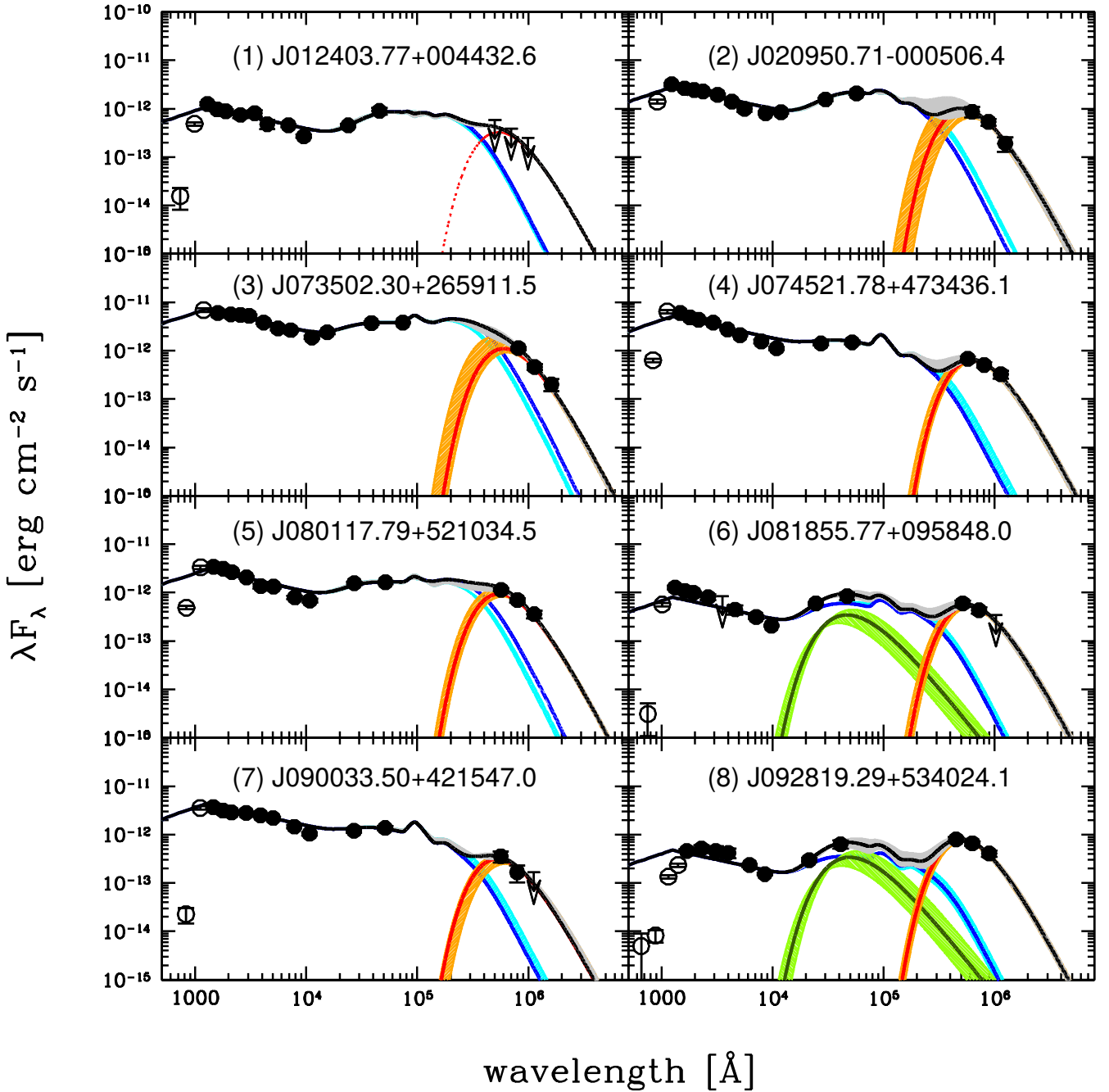
Fig. 5. Resulting rest-frame SED decompositions for half of the sources (continues in Fig. 6). Black circles are the rest-frame photometric points corresponding to the observed bands used to constrain the SED. Black open circles represent the photometric points not included in the fits (at $\lambda < 1216$ Å due to Ly-α absorption, see the text for more details), while the black arrows correspond to upper limits on the observed flux densities at 1σ. Lines (and shaded areas) correspond to the model templates (and the 1σ error) found as best-fit solution to describe the photometric points through the χ^2 minimisation: blue is the accretion disc plus torus template (AD + T), red is the cold dust component (CD) while dark green is the NIR excess (NE) when present. Finally, the black line shows the sum of all these contributions. Blue, orange, and light green shaded areas correspond to the accretion disc plus torus, the cold dust, and the NIR excess templates within 1σ of the best-fit template, and light grey shaded area to their sum.

computation of the bolometric luminosity, we do not account for the soft X-ray emission, which has been demonstrated to be negligible. In fact, the bolometric corrections, that is, the ratio between the bolometric luminosity and the luminosity at a specific wavelength, found in the soft X-ray band are quite large, of the order of 20–30, as in Marconi et al. (2004) and Lusso et al. (2012), for instance.

Similarly, the quasar monochromatic luminosities at 2500 Å, 4500 Å and 6 μm and the luminosity at 158 μm (which

corresponds to CII emission line), were computed as:

$$\lambda L_\lambda = 4\pi d_L^2 \, \lambda f(\lambda) \ [\text{erg/s}] \tag{7}$$

where $f(\lambda)$ was obtained by interpolating the best-fit model accretion disc plus torus template (for $L_{2500\,\text{Å}}$, $L_{4500\,\text{Å}}$ and $L_{6\,\mu\text{m}}$) and the total template (for $L_{158\,\mu\text{m}}$), and properly correcting for dust absorption, considering the value of the corresponding intrinsic template.
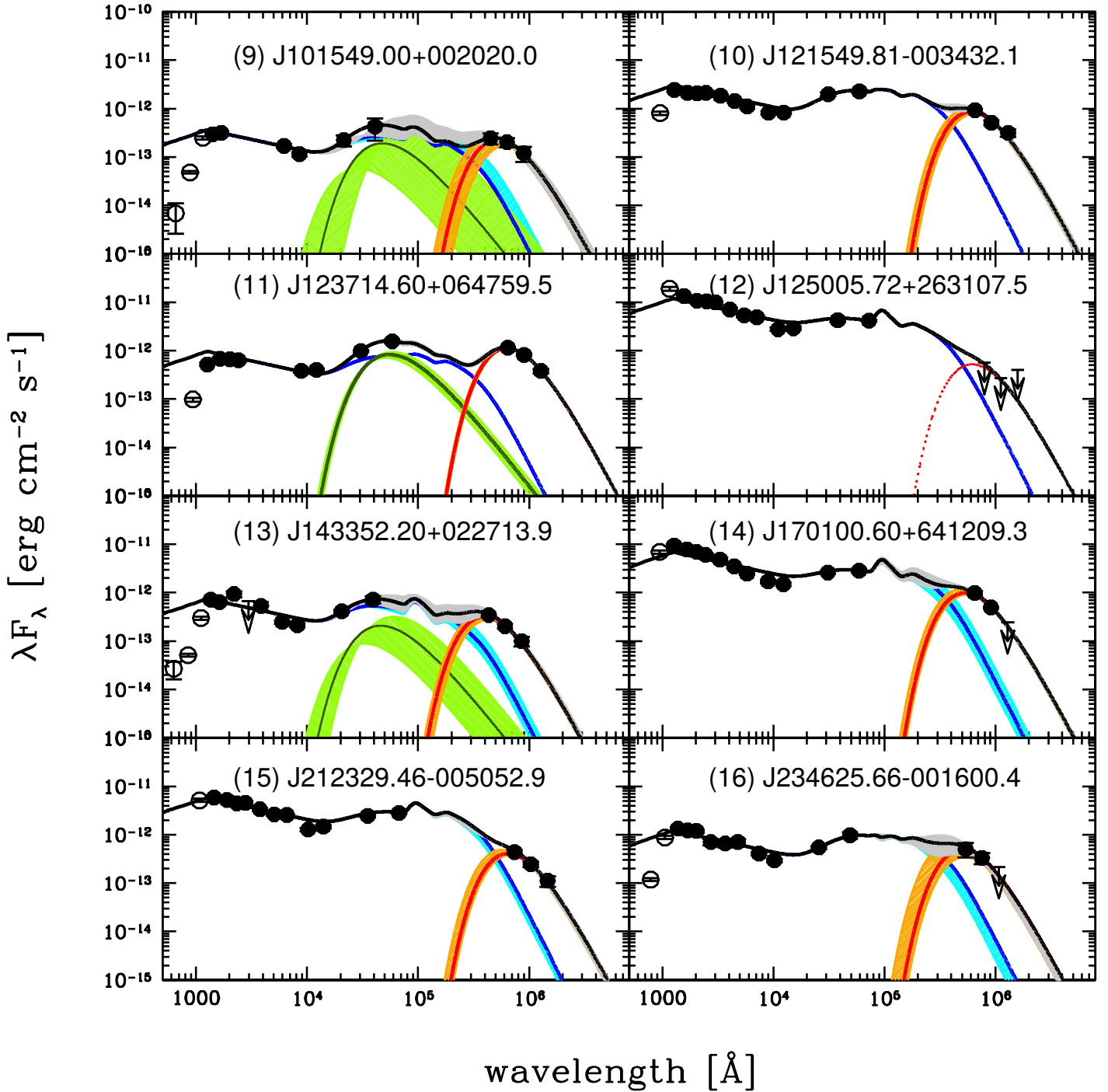
**Fig. 6.** Same as in Fig. 5 for the remaining 8 sources.

The quasar bolometric and the monochromatic luminosities computed as described above are reported in Table 5. As expected, these quasars show very high bolometric luminosities (in the range 10^{47}–10^{48} erg/s); they populate the brightest end of the luminosity function.

It is well known that the optical continuum luminosity can be used as a proxy of the quasar luminosity, while the MIR flux is directly linked to the circumnuclear hot dust emission. Moreover, the dust-covering factor for type I AGN can be obtained from the ratio between the thermal MIR emission and the primary quasar radiation. Under these assumptions, a plot such as that in Fig. 8 has been shown by Maiolino et al. (2007) to recognise a mild trend of the covering factor with the quasar

luminosity, that is, it decreases with optical luminosity. A strong trend with luminosity also emerges from our sources (blue stars in Fig. 8), which lie slightly above (by ~0.2 dex) the relation derived by Maiolino et al. (2007), however. This is not surprising since the WISSH quasars have been selected to be the most luminous in the 22 μm band, which corresponds to about ~6 μm rest-frame given their redshift.

4.2. Infrared luminosities and star formation rates

An interesting parameter to derive is the IR luminosity of the host galaxy component, which is due to the reprocessed UV
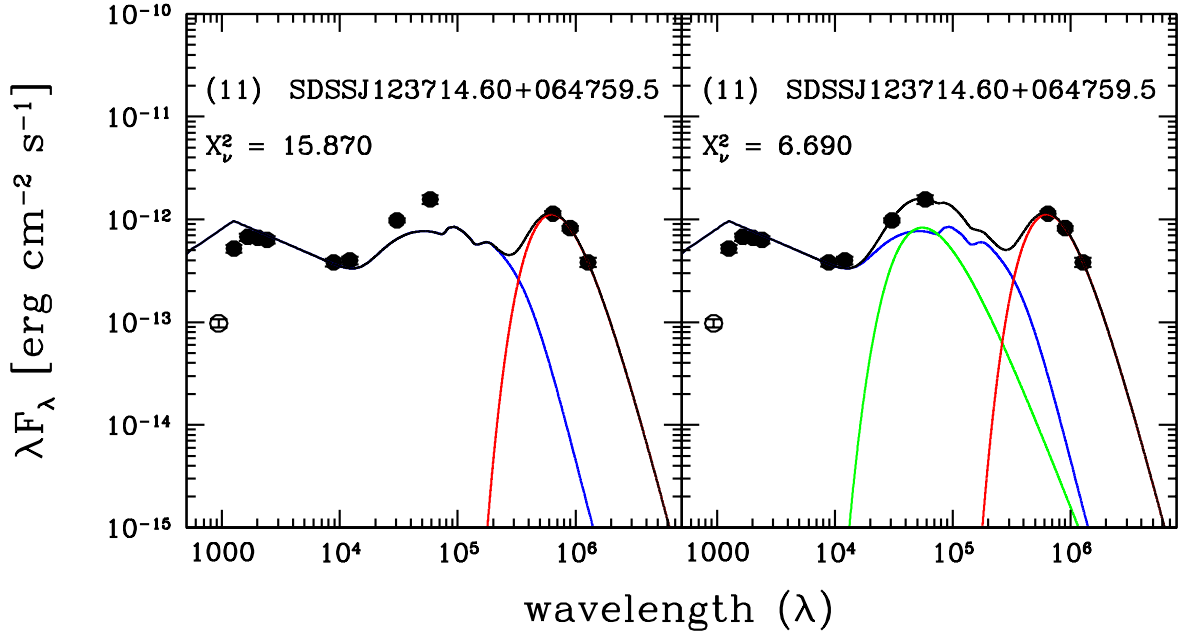
Fig. 7. Example of a fit in which an additional component (NE) has been added to fully describe the NIR emission. *The left panel* shows the standard fit with two components, while *the right panel* shows a fit in which the NIR excess blackbody is included. The *F*-test on this source shows that this component improves the fit at a ≥99% confidence level.

Table 5. Quasar bolometric luminosity and monochromatic luminosities at 2500 Å, 4500 Å, 6 μm, and 158 μm.

N	$\log(L_{\rm bol})$ [erg/s]	$\log(L_{2500\,\text{Å}})$ [erg/s]	$\log(L_{4500\,\text{Å}})$ [erg/s]	$\log(L_{6\,\mu m})$ [erg/s]	$\log(L_{158\,\mu m})$ [erg/s]
1	47.54	47.05	46.93	47.10	45.73
2	47.64	47.15	47.03	47.19	45.84
3	47.65	47.16	47.04	47.05	45.77
4	48.03	47.54	47.41	47.15	46.05
5	47.80	47.31	47.18	47.22	46.05
6	47.36	46.87	46.75	46.87	46.00
7	47.98	47.49	47.36	47.10	45.52
8	47.31	46.82	46.70	46.83	46.15
9	47.20	46.71	46.58	46.71	45.65
10	47.62	47.13	47.00	47.17	45.94
11	47.15	46.66	46.53	46.71	46.15
12	47.92	47.43	47.30	47.15	45.45
13	47.56	47.07	46.94	47.03	45.42
14	47.98	47.49	47.36	47.27	45.83
15	47.71	47.22	47.10	47.09	45.54
16	47.50	47.01	46.88	47.06	45.69

stellar emission by dust and indeed depends on both the physical properties of the dust (i.e. mass) and of the incident radiation (i.e. SF and the quasar, see discussion in Sect. 4.2).

We computed the SFR using the relation by Kennicutt (1998) scaled to a Chabrier IMF:

$$SFR(M_\odot/\text{yr}) = 10^{-10} L_{\rm IR\,8-1000\,\mu m}^{\rm Host} \ (L_\odot) \tag{8}$$

where the IR host galaxy luminosity ($L_{\rm IR}^{\rm Host}$) was obtained by integrating the best-fit modified blackbody in the range 8−1000 μm:

$$L_{\rm IR\,8-1000\,\mu m}^{\rm Host} = 4\pi d_L^2 \int_{8\,\mu m}^{1000\,\mu m} B\, f_{\rm CD}\ [\text{erg/s}]. \tag{9}$$

Both $L_{\rm IR\,8-1000\,\mu m}^{\rm Host}$ and SFR are given in Table 6, while B is the normalisation related to the CD template. The values of SFR

found for these sources are extremely high (>400 $M_\odot$/yr and up to ~4500 $M_\odot$/yr).

These derived SFR values assume that all the FIR emission comes from young stars. However, we know that this is not completely true since the quasar emission might contribute to it (Schneider et al. 2015; Symeonidis 2017). For this reason, the SFR values reported in the table have to be considered as upper limits. A more detailed discussion on this can be found in Sect. 4.2, where the quasar contribution to the FIR radiation is accounted for in a statistical way.

While there is broad consensus that the strong NIR emission observed in quasars is due to the central source, the debate is still on whether the FIR emission is mainly powered by the starburst, or if quasars are required as an additional energy source.

We estimated the possible contribution of the quasar to the heating of the dust in the host galaxy using the same approach
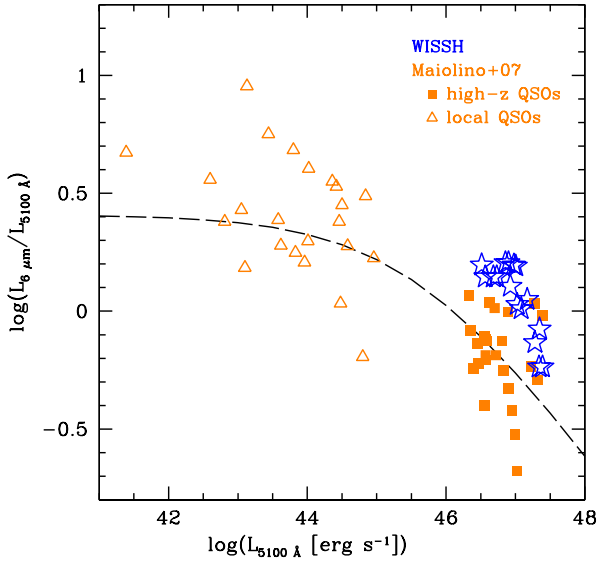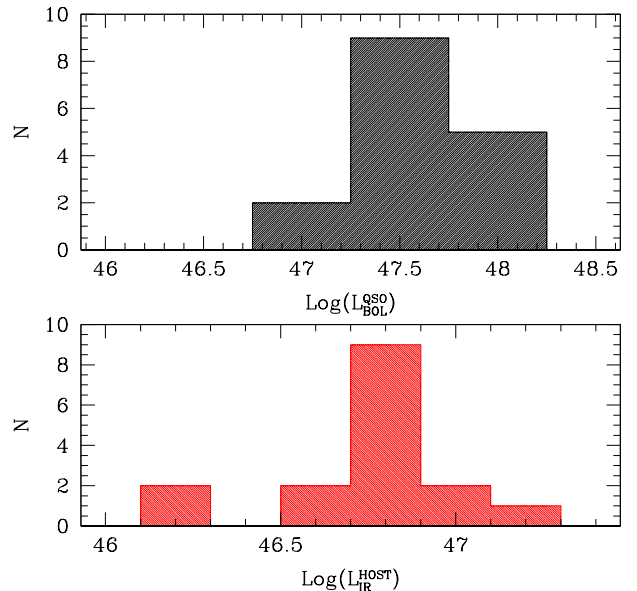
Fig. 8. MIR-to-optical continuum luminosity versus optical continuum luminosity. The WISSH quasars are the blue stars in the plot, while we plot in orange the sample from Maiolino et al. (2007) of high-z (squares) and local (triangles) sources. The dashed black line is the relation derived by Maiolino et al. (2007).

as in Schneider et al. (2015). For the $z = 6.4$ quasar SDSS J1148+5251, they modelled the dust in the host with a spheroidal inhomogeneous distribution extending from just outside the quasar dusty torus up to a few kpc. A central source was included, with a bolometric luminosity sufficient to match the observed optical data; the quasar SED was chosen from a few templates including the contribution of the dusty torus in the MIR. The heating of the dust in the host by the central source (and by an additional contribution from stars in the galaxy) was computed using the radiative transfer code TRADING (Bianchi 2008), assuming the typical properties of dust in the Milky Way (Draine & Li 2007). From their simulations, Schneider et al. (2015) concluded that dust in the host galaxy, heated by the IR radiation from the dusty torus, can contribute significantly (at least for 30% and up to 70%) to the FIR SED of the quasar-host system.

We repeated the same procedure here for two extreme sources in our sample: the least (SDSS J123714.60+064759.5) and the most (SDSS J074521.78+473436.1) luminous ones. Given the importance of such an estimate, we will apply the same procedure for the whole sample in the future. For the two sources in this work, we produced TRADING radiative transfer simulations, choosing as the central source the nuclear and torus emission best-fit templates obtained from the optical/NIR data as described in Sect. 3. We adopted the same dust distribution and mass as in Schneider et al. (2015): as we show in the next section, the dust masses in our sample are of the same order of the mass for SDSS J1148+5251, studied by Schneider et al. (2015). By comparing the modelled and observed SED, we found that the quasar contribution to the FIR fluxes is about 43% in the least luminous source, which increases to 60% for the most luminous source. This points towards a mild trend with luminosity. However, considering that the bolometric luminosities are homogeneously distributed, as visible in Fig. 9, we can assume an average quasar contribution of ~50% to the total FIR luminosity, which also accounts for the uncertainties in the radiative transfer model. The quasar-corrected infrared luminosities and SFR

Table 6. Infrared luminosity computed by integrating the host emission from $8\,\mu$m to $1000\,\mu$m, related SFRs from Kennicutt (1998), and FIR luminosity of the host component from $40\,\mu$m to $120\,\mu$m.

| N	$\log(L_{\mathrm{IR}\,8-1000\,\mu m}^{\mathrm{Host}})$ [erg/s]	SFR [$M_\odot$/yr]	$\log(L_{\mathrm{FIR}\,40-120\,\mu m}^{\mathrm{Host}})$ [erg/s]
1	<46.72	1400	46.59
2	46.87	2000	46.73
3	46.55	930	46.44
4	46.83	1800	46.72
5	47.01	2700	46.88
6	46.90	2100	46.78
7	46.54	910	46.41
8	47.24	4500	47.09
9	46.70	1300	46.56
10	46.77	1600	46.66
11	46.92	2200	46.81
12	<46.21	<410	<46.10
13	46.90	2000	46.61
14	46.85	1800	46.71
15	46.27	490	46.17
16	46.79	1600	46.64

Fig. 9. Distribution of the bolometric luminosities (*upper panel*) and of the host IR luminosities (*lower panel*) of the sample.

can therefore be derived by simply dividing the values given in Table 6 by a factor of 2.

4.3. Star formation rate vs. black hole accretion

Figure 10 shows the IR luminosity that is due to SF (hereafter SF luminosity) versus the quasar bolometric luminosity. As expected, the WISSH quasars (blue stars) populate an extreme region of this plane. In the same figure we also show as red asterisks, the SF luminosity values statistically corrected for the quasar contribution. Such extreme values are in perfect agreement with the results found for quasars at high z with similar properties, such as the two samples presented by Netzer et al. (2014, 2016), and the hot dust obscured galaxies (from the work by Fan et al. 2016), shown in Fig. 10 as magenta pentagons, cyan triangles, and orange squares, respectively.
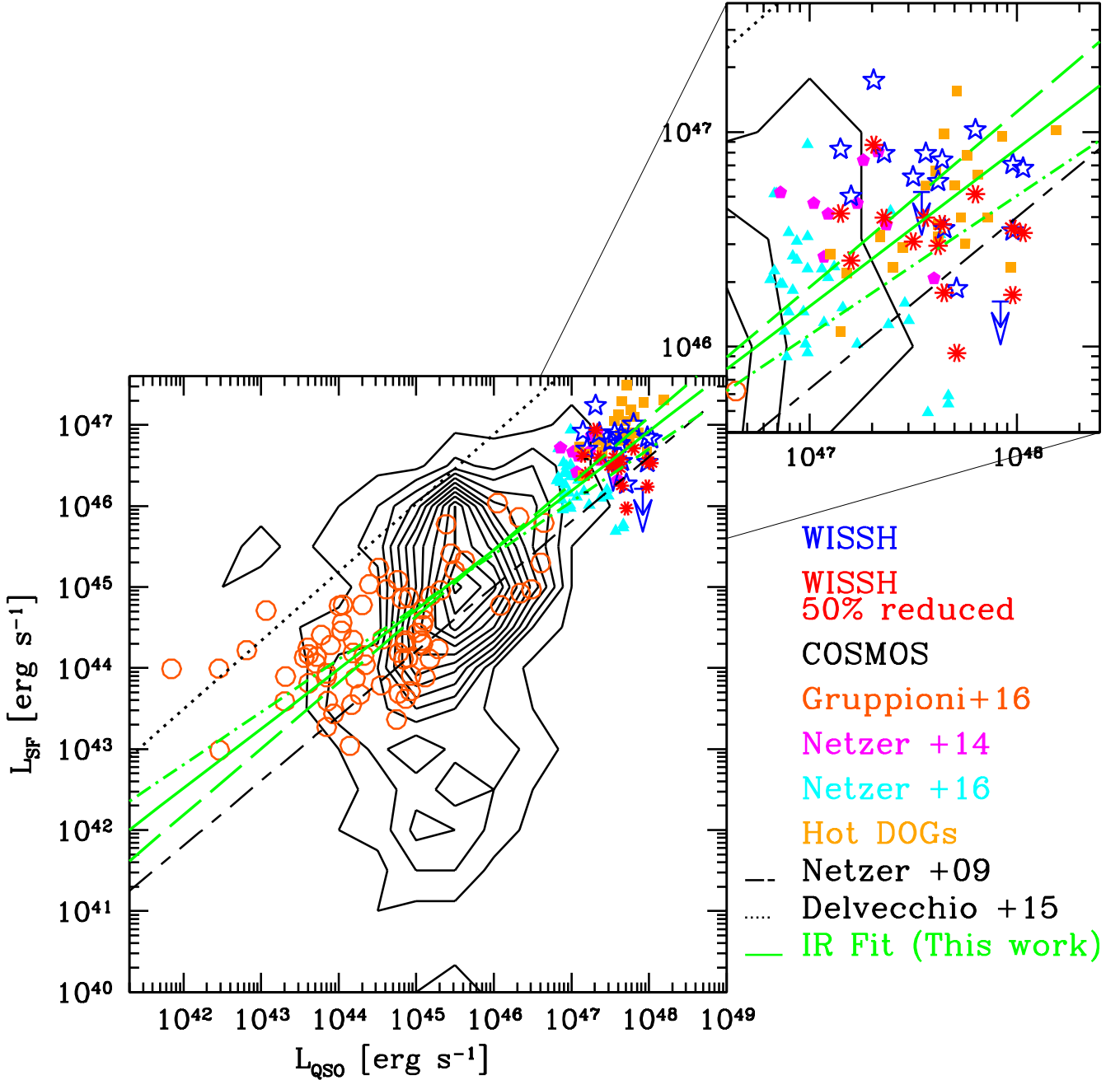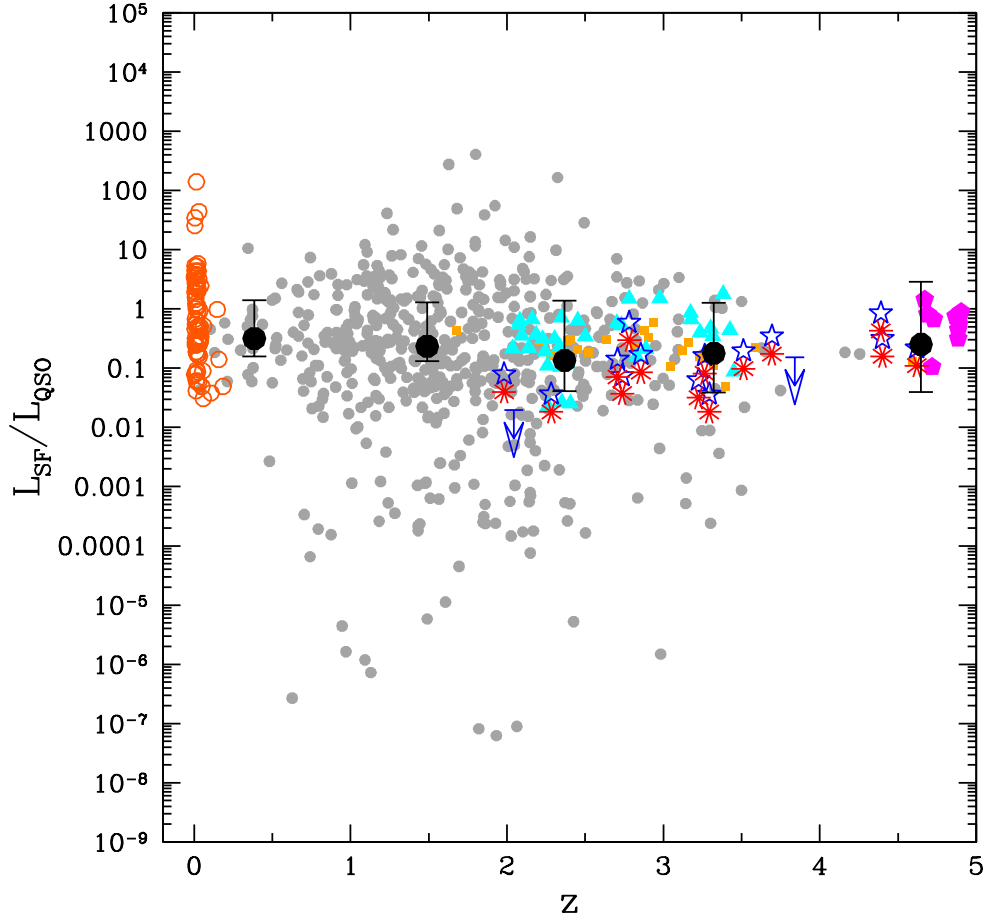
Fig. 10. SF luminosity vs. quasar bolometric luminosity for the WISSH quasars in comparison with other samples. The 16 WISSH quasars are shown as blue stars in the plot, while the red asterisks show SF luminosity values reduced by a factor of about 2 to account for the quasar contribution to the FIR. The same correction has been applied to the samples from Netzer et al. (2014, 2016) and Fan et al. (2016), which are of the same luminosity range.

For three objects in our sample in common with Netzer et al. (2016), we can directly compare the values of SFR. These are SDSS J020950.71-000506.4 (2) with an SFR of 1700 $M_\odot$/yr from Netzer et al. (2016) and of 2000 $M_\odot$/yr from our analysis, SDSS J123714.60+064759.5 (11), which has 2700 $M_\odot$/yr and 2200 $M_\odot$/yr in the two works, and SDSS J212329.46-005052.9 (15), with 300 $M_\odot$/yr and 490 $M_\odot$/yr, respectively.

Previous studies about a possible correlation between the SF activity and the quasar luminosity led to discrepant results. Several works based on X-ray data revealed the presence of a robust correlation at high redshift and quasar luminosity, which weakens or disappears for sources at lower redshift and luminosity. In particular, Stanley et al. (2015), Harrison et al. (2012), and

Rosario et al. (2012), who examined data obtained via stacked photometry, found a flat distribution of $L_{SF} - L_{QSO}$. However, Dai et al. (2015), for a sample of FIR-detected quasars at $0.2 < z < 2.5$, found a significant trend between these two parameters over four orders of magnitude in luminosity. As noted in several previous works (see e.g. Netzer et al. 2016), these discrepancies might be attributed to different selection criteria and/or methods of analysis. In particular, Dai et al. (2015) have been able to reconcile their results with those obtained by Stanley et al. (2015), by considering stacked IR values.

Given the limited luminosity range spanned by our sample, we are not able to determine any possible $L_{SF} - L_{AGN}$ trend. In Fig. 10 we report the local sample of IR-selected galaxies from

Fig. 11. Ratio between SF and quasar bolometric luminosities as a function of redshift for the same sources as presented in Fig. 10. Black points represent the median value in a redshift bin.

Gruppioni et al. (2016) shown as brown circles and the quasar sample from the COSMOS survey (Bongiorno et al. 2012), reported with density contours. The combination of these samples allows us to span a wide range of luminosity and redshift. Very high L_{QSO} objects are indeed missing from studies based on small fields, like COSMOS, which do not properly sample the bright end of the quasar luminosity function. The plot clearly shows that at high luminosities (both bolometric and SF luminosity), there is a smaller dispersion in luminosity than what is found for less luminous samples. Quantitatively, the highly luminous sources have a dispersion that is 2.15 times smaller than the lowly luminous ones. However, it is worth noting that all the aforementioned samples are *Herschel*-detected, except for COSMOS.

We investigated whether there is an hidden redshift dependence in the relation $L_{SF} - L_{QSO}$. Figure 11 shows the ratio between the SF and the quasar bolometric luminosity versus z, for the same samples of Fig. 10 (with COSMOS in grey points). Black points represent the median values in bins of redshift with associated errors, which were computed considering the differences between the first and third quartiles and the median value (or second quartile) of the set of data. As is clearly visible, there is no sign of strong trend with redshift, which allows us to use samples at different redshifts to derive a relation between the SF and the quasar activity for the IR sources.

Here we concentrate on the *Herschel*-detected samples, that is, the local sample from Gruppioni et al. (2016, orange squares), the $z > 2$ samples from Netzer et al. (2014, magenta pentagons)

and Netzer et al. (2016, cyan triangols), the Hot DOGs from Fan et al. (2016, orange squares) and the WISSH sample (red asterisks) at $1.9 < z < 4.6$. For these samples we have obtained a fit that is reported as a green solid line in Fig. 10, for which we assumed the same correction for the quasar contamination to the FIR (50%) as for the measurements belonging to the samples from Netzer et al. (2014, 2016) and from Fan et al. (2016), which have similar properties. In contrast, we cannot make the same assumption for the objects by Gruppioni et al. (2016): these are local sources at lower luminosity, therefore the quasar contribution to the FIR may be different compared to high-luminous sources. To be more accurate, we calculated the bisector of the two regression lines by first treating L_{QSO} (dashed green line) as the independent variable and then considering the SF luminosity L_{SF} as the independent variable (dot-dashed green line). The bisector, the green straight line in the plot, has a dispersion of 0.39 dex and presents the following form:

$$\log\left(\frac{L_{SF}}{10^{44}\ \mathrm{erg/s}}\right) = \log\left(\frac{L_{QSO}}{1.82 \times 10^{44}\ \mathrm{erg\ s^{-1}}}\right)^{0.73} \quad (10)$$

and it can be directly compared with the relation found by Delvecchio et al. (2015 $L_{SF} \propto L_{BOL}^{0.85}$) for their SF-dominated sources (i.e. those with $L_{SF} > L_{QSO}$) at $1.5 < z < 2.3$ and with the relation obtained by Netzer (2009) for quasar-dominated sources ($L_{SF} \propto L_{BOL}^{0.78}$).

As expected, this relation differs significantly from the relation of Delvecchio et al. (2015), while it is in much better
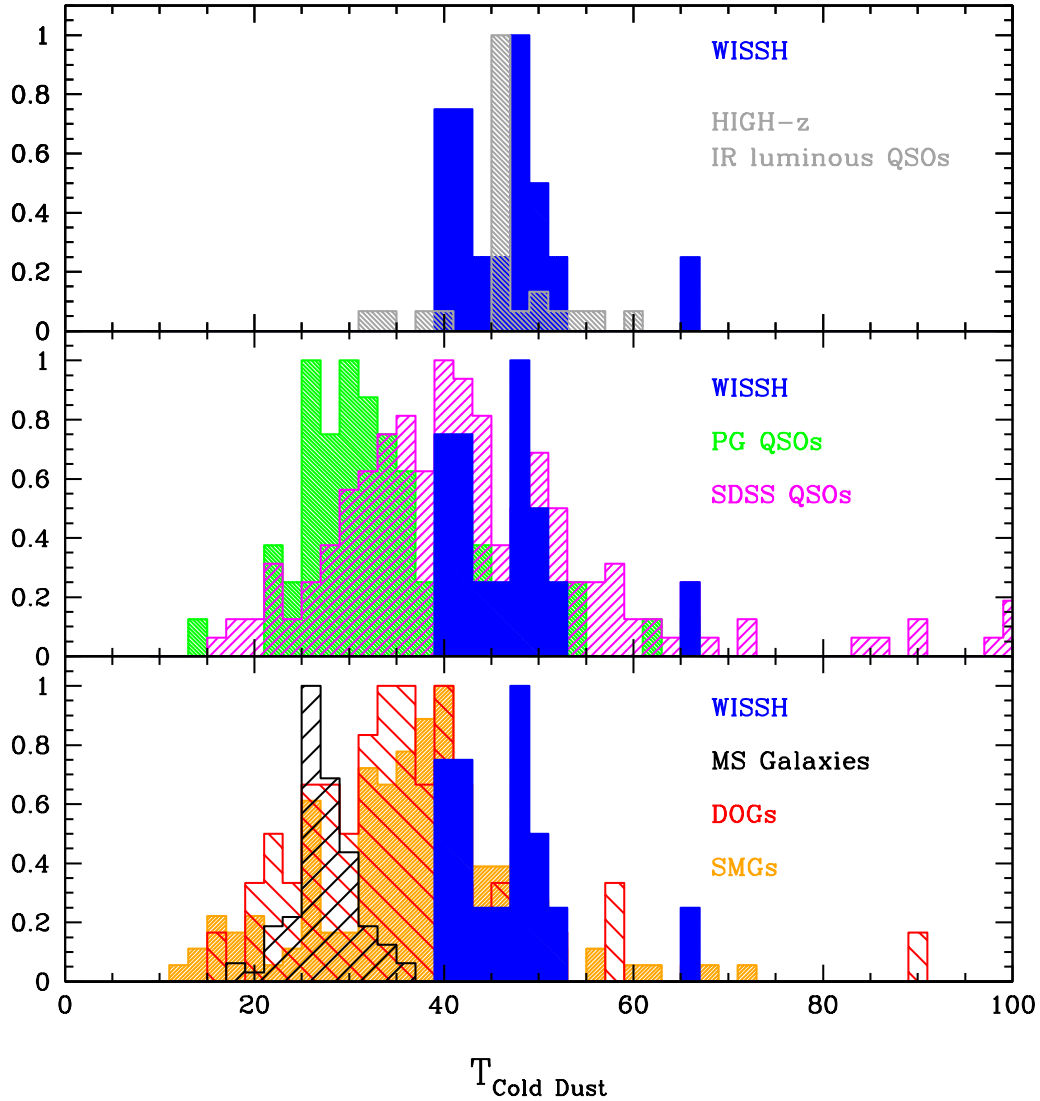
Fig. 12. Temperature distribution of the cold dust for the WISSH quasars (blue) compared to: high-z IR luminous quasars from Beelen et al. (2006), Leipski et al. (2014), Valiante et al. (2011) (*upper panel*); local PG quasars from Petric et al. (2015) and SDSS quasars at $z < 4.7$ from Ma & Yan (2015) (*central panel*); and galaxies from Magdis et al. (2012), Santini et al. (2014), Melbourne et al. (2012), Chapman et al. (2005), Magnelli et al. (2014), Miettinen et al. (2015) (*lower panel*). Note that all these works have assumed different values of both the coefficient of the modified blackbody β and the dust absorption coefficient k_0.

agreement with the relation derived by Netzer (2009), especially at the high-luminosity end. At lower luminosities, in contrast, the newly derived relation is flatter than the relation reported by Netzer (2009) one, with a slope of 0.73 instead of 0.78. The difference can be attributed to the fact that our relation has been derived considering only *Herschel*-detected sources, while the relation published by Netzer (2009) is mainly based on optically selected SDSS sources.

4.4. Dust temperatures and masses

4.4.1. Cold dust

Under the assumption that the dust emissivity can be described as a simple frequency power-law, and assuming that dust is in thermal equilibrium, we can also derive some dust properties from the result of the SED fitting, in particular its mass and temperature. More specifically, the FIR emission is linked to the cold dust component that is present on the galaxy scale while

the NIR emission is related to the hot dust component close to the nucleus in the torus. Following Wien's displacement law, we know that the peak of the blackbody component is strictly connected to the temperature of the emitting dust grains. We have underlined the fact that the real SEDs of galaxies cannot be described by a single-temperature modified blackbody because grains of different sizes and shapes give birth to a non-trivial distribution of temperatures. However, for simplicity, a blackbody (or a modified blackbody) component or a grid of templates (as in Chary & Elbaz 2001 and Dale et al. 2014) that is also characterised by a single-temperature emission, is commonly used to describe the IR radiation (see e.g. Leipski et al. 2013; Netzer et al. 2016).

Figure 12 shows the distribution (normalised for the maximum value) of the temperatures of the cold dust component found for our objects (blue histogram), ranging from about $T = 40$ K to $T = 50$ K, in good agreement with the results of previous studies of high-redshift, IR luminous quasars (e.g. Beelen et al. 2006; Leipski et al. 2014; Valiante et al. 2011), as

Table 7. Cold and hot dust masses computed as described in Sect. 4.4.

N	Cold T_d [K]	Cold M_d [$10^8 M_\odot$]	Hot T_d^{Ex} [K]	Hot M_d^{Ex} [$M_\odot$]	Hot M_d^{TOT} [$M_\odot$]
1	48	1.9	–	–	130
2	49	2.5	–	–	190
3	43	2.5	–	–	240
4	41	6.1	–	–	72
5	47	4.3	–	–	90
6	45	4.3	790	57	85
7	49	1.2	–	–	84
8	51	4.6	742	106	210
9	50	1.5	786	51	51
10	43	4.1	–	–	156
11	41	7.5	664	134	170
12	42	1.4	–	–	237
13	66	0.5	814	54	69
14	49	2.3	–	–	169
15	41	1.9	–	–	196
16	52	1.5	–	–	145

Notes. We report both the total hot dust mass and the excess found for our sources alone. The 11 sources with no additional NIR BB component have no estimates of the hot dust mass excess.

visible in the upper panel. The central and lower panels show as a comparison the distribution of cold dust temperatures found for different classes of objects. It is important to note that all these works have assumed different values of both the coefficient of the modified blackbody β and the dust absorption coefficient k_0. In the central panel we report the WISSH sources compared to the local ($z < 0.5$) PG quasars from Petric et al. (2015) and the SDSS optically selected quasars at $z < 4.7$ from Ma & Yan (2015). The different IR luminosity ranges directly translate into a different dust temperature distribution, meaning that while the less luminous PG quasars have lower temperatures (in the range 20–50 K) than the WISSH sample, the SDSS objects show a wider distribution, with the bulk peaking at higher value (~40 K) than the PG quasars, and with the warmer tail of the distribution comparable to ours. For the same reason, WISSH quasars show dust temperatures that are much higher than the bulk of the galaxy population, as clearly shown in the lower panel of Fig. 12, where they are compared to normal galaxies, that is, to the sample of main sequence galaxies from Magdis et al. (2012) and Santini et al. (2014), the dust obscured galaxies (DOGs) from Melbourne et al. (2012) and the submillimiter galaxies (SMGs) from Chapman et al. (2005), Magnelli et al. (2014), and Miettinen et al. (2015).

With the previously derived $L_{IR\,8-1000\,\mu m}^{Host}$, it is also possible to obtain a measure of the mass associated with the cold dust component (cold M_d) using the formula derived by Hughes et al. (1997) (see also Berta et al. 2016, for a detailed derivation):

$$M_d = \frac{L_{IR\,8-1000\,\mu m}^{Host}}{4\pi \int k_d(\nu)\,B(\nu,T_d)\,d\nu} \quad (11)$$

which is valid under the assumption that the emission is optically thin with optical depth $\tau \ll 1$.

In the above formula, $B(\nu,T_d)$ is the Planck function for dust with a temperature T_d, determined by the best-fit, and $k_d(\nu) = k_0 (\nu/\nu_0)^\beta$ with k_0 the absorption coefficient and ν_0 the frequency at which $\tau = 1$. Following Beelen et al. (2006), here we assume $k_0 = 0.4$ [cm^2/g] and $\nu_0 = 1200\,\mu m$. The dust mass therefore depends on the IR luminosity (SFR) of the source and the temperature of the dust grains, meaning that for a given temperature, there is a linear relation between dust mass and SFR.

The derived masses, reported in Table 7, are of the order of $10^8 M_\odot$, in agreement with previous studies on high-z IR luminous sources (e.g. Beelen et al. 2006; Wang et al. 2008; Banerji et al. 2017; Valiante et al. 2011; Ma & Yan 2015).

4.4.2. Hot dust

As we mentioned in Sect. 3.2.3, some of our sources (31%) show an NIR excess in their SED that requires a component in addition to the classical torus models (Stalevski et al. 2012, 2016). The presence of such component has been noted in several previous works on luminous quasars, but the physical origin of this component is not yet clear. Edelson & Malkan (1986) were the first to note the need of an additional NIR component that peaks at about $5\,\mu m$, corresponding to a dust temperature of about 600 K. More recently, Mor et al. (2009), analysed a sample of Spitzer-selected low-z quasars with luminosities ranging from $44.6 < \log(L_{bol}) < 46.8$. They found that their objects require two additional dust components to fit the NIR emission. The first component (very hot dust component) has temperatures ranging from 900 K to 1800 K, and the second (warm dust component) has 200 K. Similarly, Hernán-Caballero et al. (2016) found a peak in the distribution of the very hot dust temperatures at about 1180 K and of the warm temperatures at 400 K for a sample of luminous quasars at $z < 3$. While the warm component has been interpreted as dusty clouds in the narrow line region, the very hot dust emission might be related to graphite clouds located at the edge of the dusty torus, thus inside the sublimation radius of silicate (whose sublimation temperature is lower than for pure graphite grains), but outside the broad line region. However, as the NIR SED of the total quasar emission (disc plus dust) is strictly connected to the spectral shape assumed for the NIR spectrum of the disc, the resulting excess components are somewhat model dependent.

As shown in Table 7, we found a NIR excess for the WISSH sample corresponding to dust with temperatures ranging from $T = 650$ K to $T = 850$ K. Such values are in agreement with the result from Edelson & Malkan (1986), but in between the results found by Mor et al. (2009) and Hernán-Caballero et al. (2016).

It is worth noting that this further component peaks at about $22\,\mu m$ rest-frame, where the sources in the sample have been selected to be the brightest. This excess is a sign of the fact that our sources show more hot dust than that is present in the torus models. Moreover, they may have a large covering factor, allowing clouds to intercept more continuum radiation.

Furthermore, from the NIR excess emission component, we also estimated the mass of the additional hot dust found. Differently from the cold dust component, which is described as a greybody, the hot dust emission excess was fitted with a single-temperature blackbody. Therefore it is in principle not possible to compute the hot dust mass using the previous relation. However, following Jiang et al. (2006), we approximated the hot dust emission as a greybody with $k_0 = 2.06 \times 10^3$ [cm²/g]. Since in a greybody the emissivity α is below 1, these values have to be considered as lower limits and are in agreement with the values found in the aforementioned work.

Finally, we also computed the total hot dust mass for all sources (hot $M_{\rm d}^{\rm TOT}$) by fitting the photometric points from the UV to the NIR with a combination of pure accretion disc (Feltre et al. 2012) and single-temperature black body templates to describe the whole NIR emission.

The values of the total hot dust masses, ranging from tens to hundreds of solar masses, are given in Table 7 together with the masses associated with the excess for the five sources that require this component.

5. Conclusions

We studied a sample of hyper-luminous quasars, selected by cross-correlating data from the SDSS and the WISE All-Sky Survey, and we focused on 16 sources with *Herschel*/SPIRE data coverage.

Thanks to the multi-wavelength coverage, we were able to analyse in detail the source SEDs, fitting the observed fluxes with a multi-component model, based on a combination of quasar and host-galaxy emission emerging in the IR (where the reprocessed stellar light is re-emitted by the dust). The quasar emission was described using a combination of power laws for the primary source (Feltre et al. 2012) and the model by Stalevski et al. (2016) for the smooth and clumpy dusty torus, while the galaxy cold dust emission in the infrared bands was modeled as a modified blackbody. However, we found that in some cases, our sources show peculiar features in their SED that cannot be described by the standard modelisation. In other words, a further component, in the form of a pure blackbody, is necessary to reproduce their NIR emission. Through the SED multi-components fitting method we were able to derive robust measurements of both the quasar (i.e. bolometric and monochromatic luminosities) and the host galaxy properties (i.e. dust mass, SFRs).

Our main findings can be summarised as follows:

– The WISSH quasars populate the brightest end of the luminosity function with very high bolometric luminosities, $L_{\rm BOL} > 10^{47}$ erg/s. They are hosted in galaxies with extremely high SFRs of up to $4500\,M_\odot$/yr. Since the quasar light might contaminate the FIR emission, following Schneider et al. (2015), we estimated its possible contribution to the heating of the dust in the host galaxy, taking as test cases the least and the most luminous sources of the sample. We found that the quasar contribution to the FIR fluxes is about 43% in the least luminous source, which increases to 60% for the most luminous source. Considering that the

bolometric luminosities are homogeneously distributed, we therefore assumed an average quasar contribution of ~50% to the total FIR luminosity. Even accounting for this correction, the SFRs of the sources still remain of the order of thousands $M_\odot$/yr.

– By combining our sample with both high-z hyper-luminous quasars (Netzer et al. 2014, 2016) and local quasars from Gruppioni et al. (2016) and the quasar sample from the COSMOS survey (Bongiorno et al. 2012), from the $L_{\rm SF} - L_{\rm QSO}$ plane a narrower (2.15 times smaller) dispersion at high quasar and SF luminosities emerges than what was found for lower values of both bolometric and SF luminosities. Using only the *Herschel*-detected samples we derived a log-linear relation between the SF and the quasar luminosities, $L_{\rm SF} \propto L_{\rm QSO}^{0.73}$, which is flatter than the relation derived for optically selected type II AGN by Netzer (2009).

– While most of the WISSH quasars are well described by a standard combination of accretion disc plus torus and cold dust emission, for ~31% of them, an additional hotter component is required to reproduce the observed fluxes. The peak of this emission falls roughly at about $22\,\mu m$ rest-frame, where the sources in the sample have been selected to be the brightest, and it has temperatures ranging from $T = 650\,K$ to $T = 850\,K$.

– The temperature of the cold dust component has a peak at about $50\,K$, in agreement with previous studies of high-z IR luminous quasars (Beelen et al. 2006; Leipski et al. 2014; Valiante et al. 2011) and much higher than main-sequence galaxies. The thermal emission of the cold dust component is associated with a dust mass of the order of $10^8\,M_\odot$, which is in good agreement with previous works on high-z quasars (e.g. Beelen et al. 2006; Wang et al. 2008; Banerji et al. 2017; Valiante et al. 2011; Ma & Yan 2015).

The WISSH quasars lie in the most extreme region of the plane $L_{\rm SF} - L_{\rm QSO}$. It is worth noting that the same locus is occupied by other hyper-luminous ($L_{\rm BOL} > 10^{47}$ erg/s) quasars collected according to the level of extinction. We can place the WISSH quasars in between the heavily dust enshrouded sources such as the WISE-selected hot dust obscured galaxies by Fan et al. (2016), Piconcelli et al. (2015) and Wu et al. (2012), the NIR-selected heavily reddened quasars by Banerji et al. (2015) and Glikman et al. (2015), and finally the blue optically selected luminous quasars (e.g. Netzer et al. 2016). However, we should keep in mind that, while both the bolometric luminosity and the extinction are instant observables, the infrared-derived SF luminosity is the result of the integration of bursts of SF that occurred over billions of years, assuming that the SF remains constant over the lifetime of the burst (Leitherer & Heckman 1995). Hence, it is difficult to gain information from the SF luminosity about the ongoing SF in the host galaxy. On the other hand, the extinction of a single galaxy is strictly linked to its merger-induced evolutionary sequence. Through the WISSH quasars we therefore witness a very peculiar phase in the quasar life, during which the dust in the host has not yet been fully cleared up. This suggests that the typical evolution timescales of the quasar feedback are much shorter than those of the host galaxy SF activity.

Signatures of ionised outflows are ubiquitously detected in WISSH quasars (see e.g. Bischetti et al. 2017; Vietri et al. in prep.). Future observations with ALMA and NOEMA will be fundamental to quantify the gas reservoir in the WISSH quasars and to reveal possible massive molecular outflows, allowing us to obtain a comprehensive view of the outflow phenomenology in

these hyper-luminous quasars, and test the impact of the quasar output on the host gas ISM and its SF efficiency.

An alternative scenario suggests that the action of the quasar outflow and the host SF might not be geometrically connected. In this sense, future spatially resolved observations will be useful to perform an accurate investigation of the ongoing SF (via spectral analysis of the narrow Hα emission line, as in Carniani et al. 2015; and Cano-Díaz et al. 2012).

These quasars are also unique laboratories for studying the properties of the interstellar medium at high redshift, as the metals and dust content of their host galaxies can provide insights into both the galaxy evolution process (e.g. SFH) and the quasar feedback effects (e.g. Valiante et al. 2011, 2014).

References

Aalto, S. 2015, in Revolution in Astronomy with ALMA: The Third Year, eds. D. Iono, K. Tatematsu, A. Wootten, & L. Testi, ASP Conf. Ser., 499, 85
Avni, Y. 1976, ApJ, 210, 642
Azadi, M., Aird, J., Coil, A. L., et al. 2015, ApJ, 806, 187
Banerji, M., Alaghband-Zadeh, S., Hewett, P. C., & McMahon, R. G. 2015, MNRAS, 447, 3368
Banerji, M., Carilli, C. L., Jones, G., et al. 2017, MNRAS, 465, 4390
Barvainis, R. 1987, ApJ, 320, 537
Beelen, A., Cox, P., Benford, D. J., et al. 2006, ApJ, 642, 694
Bendo, G. J., Griffin, M. J., Bock, J. J., et al. 2013, MNRAS, 433, 3062
Berta, S., Lutz, D., Genzel, R., Förster-Schreiber, N. M., & Tacconi, L. J. 2016, A&A, 587, A73
Bianchi, S., Giovanardi, C., Smith, M. W. L., et al. 2017, A&A, 597, A130
Bischetti, M., Piconcelli, E., Vietri, G., et al. 2017, A&A, 598, A122
Blain, A. W., Smail, I., Ivison, R. J., Kneib, J.-P., & Frayer, D. T. 2002, Phys. Rep., 369, 111
Bongiorno, A., Merloni, A., Brusa, M., et al. 2012, MNRAS, 427, 3103
Cano-Díaz, M., Maiolino, R., Marconi, A., et al. 2012, A&A, 537, L8
Carniani, S., Marconi, A., Maiolino, R., et al. 2015, A&A, 580, A102
Chapman, S. C., Blain, A. W., Smail, I., & Ivison, R. J. 2005, ApJ, 622, 772
Chary, R., & Elbaz, D. 2001, ApJ, 556, 562
Cicone, C., Feruglio, C., Maiolino, R., et al. 2012, A&A, 543, A99
Cicone, C., Maiolino, R., Sturm, E., et al. 2014, A&A, 562, A21
Ciesla, L., Boselli, A., Smith, M. W. L., et al. 2012, A&A, 543, A161
Costa, T., Sijacki, D., & Haehnelt, M. G. 2014, MNRAS, 444, 2355
Cresci, G., Mainieri, V., Brusa, M., et al. 2015a, ApJ, 799, 82
Cresci, G., Marconi, A., Zibetti, S., et al. 2015b, A&A, 582, A63
Czerny, B., & Elvis, M. 1987, ApJ, 321, 305
Dai, Y. S., Bergeron, J., Elvis, M., et al. 2012, ApJ, 753, 33
Dai, Y. S., Wilkes, B. J., Bergeron, J., et al. 2015, ArXiv e-prints [arXiv:1511.06761]
Dale, D. A., Helou, G., Magdis, G. E., et al. 2014, ApJ, 784, 83
Davies, J. I., Bianchi, S., Cortese, L., et al. 2012, MNRAS, 419, 3505
Delvecchio, I., Lutz, D., Berta, S., et al. 2015, MNRAS, 449, 373
Eales, S., Dunne, L., Clements, D., et al. 2010, PASP, 122, 499
Edelson, R. A., & Malkan, M. A. 1986, ApJ, 308, 59
Elvis, M., Wilkes, B., McDowell, J., et al. 1994, ApJS, 95, 1
Fan, L., Han, Y., Nikutta, R., Drouart, G., & Knudsen, K. K. 2016, ApJ, 823, 107
Feltre, A., Hatziminaoglou, E., Fritz, J., & Franceschini, A. 2012, MNRAS, 426, 120
Feruglio, C., Maiolino, R., Piconcelli, E., et al. 2010, A&A, 518, L155
Feruglio, C., Fiore, F., Piconcelli, E., et al. 2013, A&A, 558, A87
Feruglio, C., Fiore, F., Carniani, S., et al. 2015, A&A, 583, A99
Fiore, F., Feruglio, C., Shankar, F., et al. 2017, A&A, 601, A143
Fritz, J., Franceschini, A., & Hatziminaoglou, E. 2006, MNRAS, 366, 767
Glikman, E., Simmons, B., Mailly, M., et al. 2015, ApJ, 806, 218
González-Alfonso, E., Fischer, J., Spoon, H. W. W., et al. 2017, ApJ, 836, 11
Granato, G. L., & Danese, L. 1994, MNRAS, 268, 235
Gruppioni, C., Berta, S., Spinoglio, L., et al. 2016, MNRAS, 458, 4297
Haas, M., Klaas, U., Müller, S. A. H., et al. 2003, A&A, 402, 87
Harrison, C. M., Alexander, D. M., Swinbank, A. M., et al. 2012, MNRAS, 426, 1073
Hatziminaoglou, E., Omont, A., Stevens, J. A., et al. 2010, A&A, 518, L33
Hernán-Caballero, A., Hatziminaoglou, E., Alonso-Herrero, A., & Mateos, S. 2016, MNRAS, 463, 2064
Hildebrand, R. H. 1983, QJRAS, 24, 267
Holt, J., Tadhunter, C. N., & Morganti, R. 2008, MNRAS, 387, 639
Hönig, S. F., & Kishimoto, M. 2010, A&A, 523, A27
Hopkins, P. F., & Elvis, M. 2010, MNRAS, 401, 7
Hopkins, P. F., Hernquist, L., Cox, T. J., et al. 2006, ApJS, 163, 1
Hopkins, P. F., Hernquist, L., Cox, T. J., & Kereš, D. 2008, ApJS, 175, 356
Hopkins, P. F., Torrey, P., Faucher-Giguère, C.-A., Quataert, E., & Murray, N. 2016, MNRAS, 458, 816
Hughes, D. H., Dunlop, J. S., & Rawlings, S. 1997, MNRAS, 289, 766
Ishibashi, W., & Fabian, A. C. 2012, MNRAS, 427, 2998
Jiang, L., Fan, X., Hines, D. C., et al. 2006, AJ, 132, 2127
Kato, Y., Matsuda, Y., Smail, I., et al. 2016, MNRAS, 460, 3861
Kennicutt, Jr., R. C. 1998, ARA&A, 36, 189
King, A. 2005, ApJ, 635, L121
Krawczyk, C. M., Richards, G. T., Mehta, S. S., et al. 2013, ApJS, 206, 4
Krolik, J. H., & Begelman, M. C. 1988, ApJ, 329, 702
Lani, C., Netzer, H., & Lutz, D. 2017, MNRAS, 471, 59
Laor, A., & Draine, B. T. 1993, ApJ, 402, 441
Leipski, C., Meisenheimer, K., Walter, F., et al. 2013, ApJ, 772, 103
Leipski, C., Meisenheimer, K., Walter, F., et al. 2014, ApJ, 785, 154
Leitherer, C., & Heckman, T. M. 1995, ApJS, 96, 9
Li, A., & Draine, B. T. 2001, ApJ, 554, 778
Lusso, E., Comastri, A., Simmons, B. D., et al. 2012, MNRAS, 425, 623
Ma, Z., & Yan, H. 2015, ApJ, 811, 58
Magdis, G. E., Daddi, E., Béthermin, M., et al. 2012, ApJ, 760, 6
Magnelli, B., Lutz, D., Saintonge, A., et al. 2014, A&A, 561, A86
Maiolino, R., Shemmer, O., Imanishi, M., et al. 2007, A&A, 468, 979
Maiolino, R., Russell, H. R., Fabian, A. C., et al. 2017, Nature, 544, 202
Marconi, A., Risaliti, G., Gilli, R., et al. 2004, MNRAS, 351, 169
Mathis, J. S., Rumpl, W., & Nordsieck, K. H. 1977, ApJ, 217, 425
Melbourne, J., Soifer, B. T., Desai, V., et al. 2012, AJ, 143, 125
Menci, N., Fiore, F., Puccetti, S., & Cavaliere, A. 2008, ApJ, 686, 219
Miettinen, O., Novak, M., Smolčić, V., et al. 2015, A&A, 584, A32
Minezaki, T., Yoshii, Y., Kobayashi, Y., et al. 2004, ApJ, 600, L35
Mor, R., & Netzer, H. 2012, MNRAS, 420, 526
Mor, R., Netzer, H., & Elitzur, M. 2009, ApJ, 705, 298
Mullaney, J. R., Daddi, E., Béthermin, M., et al. 2012a, ApJ, 753, L30
Mullaney, J. R., Pannella, M., Daddi, E., et al. 2012b, MNRAS, 419, 95
Mullaney, J. R., Alexander, D. M., Aird, J., et al. 2015, MNRAS, 453, L83
Nenkova, M., Ivezić, Ž., & Elitzur, M. 2002, ApJ, 570, L9
Nenkova, M., Sirocky, M. M., Nikutta, R., Ivezić, Ž., & Elitzur, M. 2008, ApJ, 685, 160
Nesvadba, N. P. H., Lehnert, M. D., De Breuck, C., Gilbert, A. M., & van Breugel, W. 2008, A&A, 491, 407
Netzer, H. 2009, MNRAS, 399, 1907
Netzer, H., Lutz, D., Schweitzer, M., et al. 2007, ApJ, 666, 806
Netzer, H., Mor, R., Trakhtenbrot, B., Shemmer, O., & Lira, P. 2014, ApJ, 791, 34
Netzer, H., Lani, C., Nordon, R., et al. 2016, ApJ, 819, 123
Ott, S. 2010, in Astronomical Data Analysis Software and Systems XIX, eds. Y. Mizumoto, K.-I. Morita, & M. Ohishi, ASP Conf. Ser., 434, 139
Pappalardo, C., Bendo, G. J., Bianchi, S., et al. 2015, A&A, 573, A129
Pappalardo, C., Bizzocchi, L., Fritz, J., et al. 2016, A&A, 589, A11
Petric, A. O., Ho, L. C., Flagey, N. J. M., & Scoville, N. Z. 2015, ApJS, 219, 22
Piconcelli, E., Vignali, C., Bianchi, S., et al. 2015, A&A, 574, L9
Pilbratt, G. L., Riedinger, J. R., Passvogel, T., et al. 2010, A&A, 518, L1
Planck Collaboration XI. 2014, A&A, 571, A11
Planck Collaboration XIII. 2016, A&A, 594, A13
Richards, G., Lacy, M., Storrie-Lombardi, L., et al. 2006, ApJ, 166, 470
Rosario, D. J., Santini, P., Lutz, D., et al. 2012, A&A, 545, A45
Rosario, D. J., Santini, P., Lutz, D., et al. 2013, ApJ, 771, 63
Rupke, D. S. N., & Veilleux, S. 2011, ApJ, 729, L27
Sanders, D. B., Soifer, B. T., Elias, J. H., et al. 1988, ApJ, 325, 74
Sanders, D. B., Phinney, E. S., Neugebauer, G., Soifer, B. T., & Matthews, K. 1989, ApJ, 347, 29
Santini, P., Rosario, D. J., Shao, L., et al. 2012, A&A, 540, A109
Santini, P., Maiolino, R., Magnelli, B., et al. 2014, A&A, 562, A30

Schartmann, M., Meisenheimer, K., Camenzind, M., Wolf, S., & Henning, T. 2005, A&A, 437, 861
Schlegel, D. J., Finkbeiner, D. P., & Davis, M. 1998, ApJ, 500, 525
Schneider, R., Bianchi, S., Valiante, R., Risaliti, G., & Salvadori, S. 2015, A&A, 579, A60
Shao, L., Lutz, D., Nordon, R., et al. 2010, A&A, 518, L26
Silk, J. 2013, ApJ, 772, 112
Silk, J., & Rees, M. J. 1998, A&A, 331, L1
Stalevski, M., Fritz, J., Baes, M., Nakos, T., & Popović, L. Č. 2012, MNRAS, 420, 2756
Stalevski, M., Ricci, C., Ueda, Y., et al. 2016, MNRAS, 458, 2288
Stanley, F., Harrison, C. M., Alexander, D. M., et al. 2015, MNRAS, 453, 591
Stevans, M. L., Shull, J. M., Danforth, C. W., & Tilton, E. M. 2014, ApJ, 794, 75
Sturm, E., González-Alfonso, E., Veilleux, S., et al. 2011, ApJ, 733, L16
Suganuma, M., Yoshii, Y., Kobayashi, Y., et al. 2006, ApJ, 639, 46
Symeonidis, M. 2017, MNRAS, 465, 1401
Symeonidis, M., Giblin, B. M., Page, M. J., et al. 2016, MNRAS, 459, 257
Telfer, R. C., Zheng, W., Kriss, G. A., & Davidsen, A. F. 2002, ApJ, 565, 773
Tsai, C.-W., Eisenhardt, P. R. M., Wu, J., et al. 2015, ApJ, 805, 90
Valiante, R., Schneider, R., Salvadori, S., & Bianchi, S. 2011, MNRAS, 416, 1916
Valiante, R., Schneider, R., Salvadori, S., & Gallerani, S. 2014, MNRAS, 444, 2442
Veilleux, S., Rupke, D. S. N., Kim, D.-C., et al. 2009, ApJS, 182, 628
Viero, M. P., Asboth, V., Roseboom, I. G., et al. 2014, ApJS, 210, 22
Wang, R., Carilli, C. L., Wagg, J., et al. 2008, ApJ, 687, 848
Weedman, D., & Sargsyan, L. 2016, ApJ, 828, 43
Witt, A. N., & Gordon, K. D. 1996, in AIP Conf. Ser. 348, ed. E. Dwek, 230
Wright, E. L., Eisenhardt, P. R. M., Mainzer, A. K., et al. 2010, AJ, 140, 1868
Wu, J., Tsai, C.-W., Sayers, J., et al. 2012, ApJ, 756, 96
Zubovas, K., & King, A. R. 2012, in AGN Winds in Charleston, eds. G. Chartas, F. Hamann, & K. M. Leighly, ASP Conf. Ser., 460, 235